

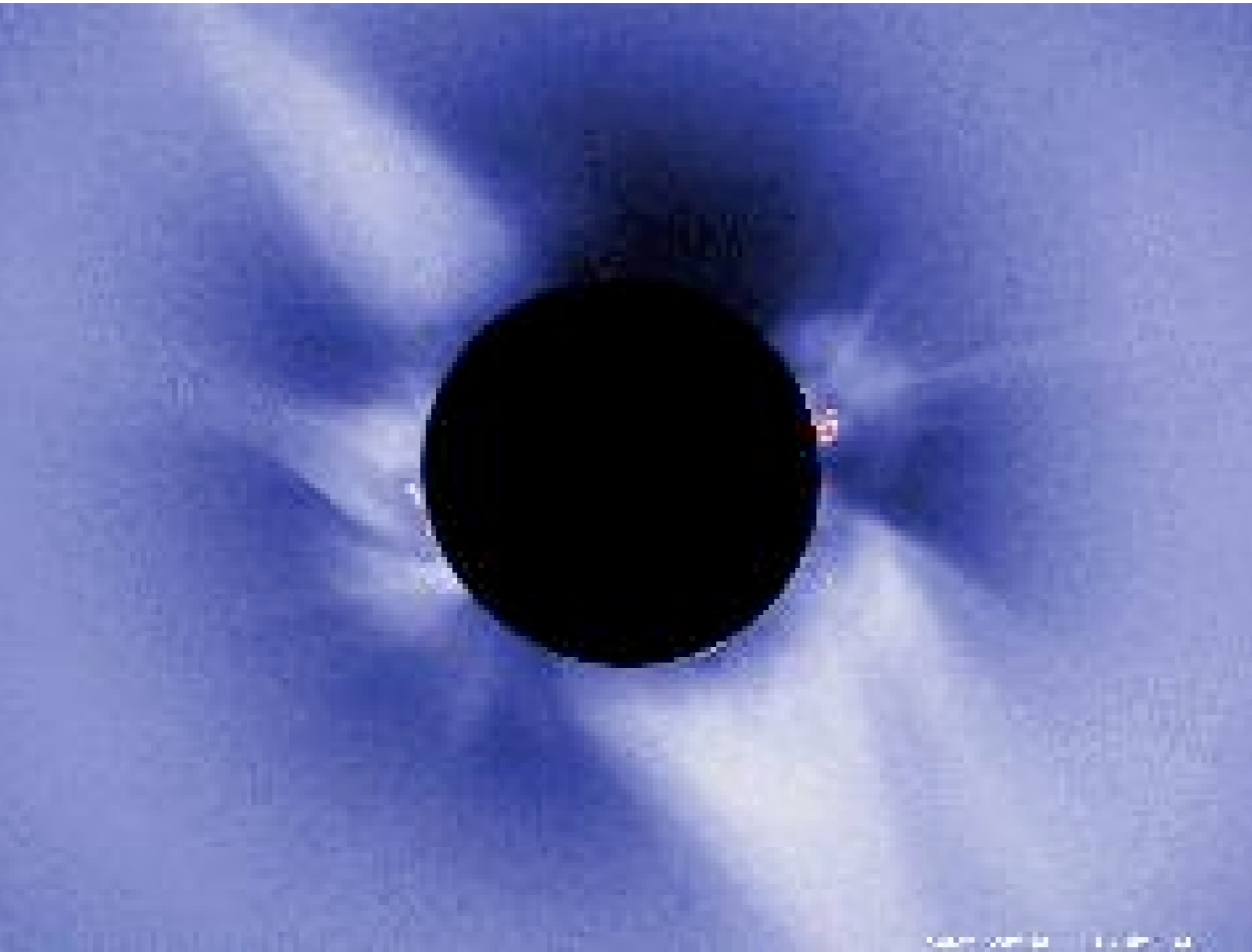
# 3D Tomographic Plasma Diagnostics for the Solar Corona

Richard A. Frazin

Dept. of Electrical and Computer Engineering

University of Illinois

Q: What is the solar corona?

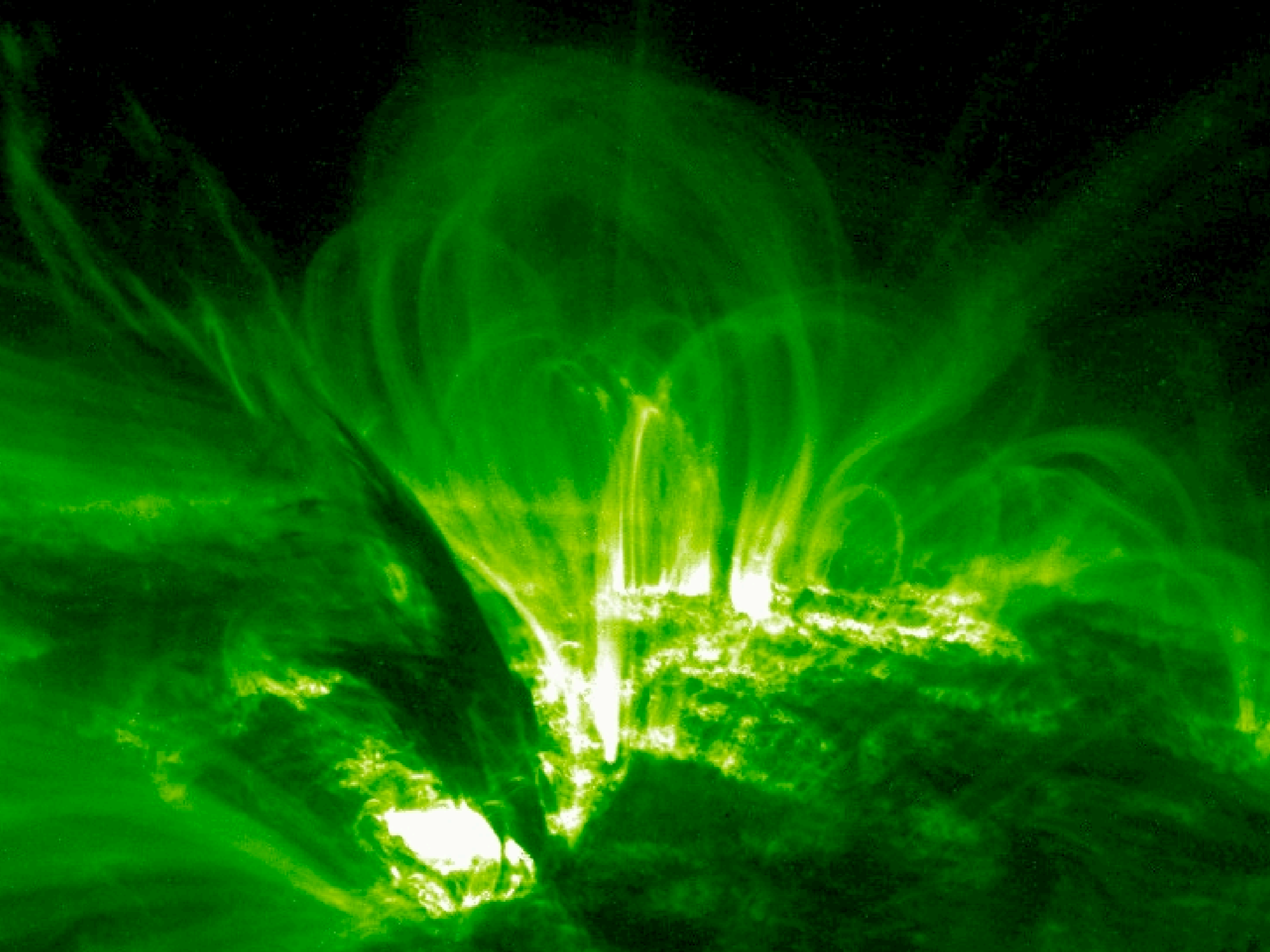


A photograph of the corona as seen during a solar eclipse. The Moon is covering optical disk of Sun.

A: It is the outermost layer of the Sun's atmosphere, with a complicated 3D structure.

# Key Points about the corona

- Sits above the photosphere, which is the predominant source of solar optical emission.
- Is the source of solar X-ray/EUV emission. Also important source of radio emission.
- Made of hot plasma,  $T = 0.5e6 - 3e6$  deg K
- This material streams out from the Sun, forming the quasi-steady solar wind
- Solar material that causes **space weather** (plasma, energetic particles) must propagate through the corona before reaching Earth.



Force Free?



**Q:** Why study the solar corona?

**A:** The solar corona presents us with a number of challenging problems in plasma astrophysics as well a number of practical issues in space weather modeling and prediction.

# Physics Issues

- Identify the processes that heat the coronal plasma
- Identify the process that accelerate it to solar wind speeds (350-850 km/s)
- Explain the rich variety of kinetic properties of coronal plasma.

# Space Weather

Sun-driven events can have important consequences for Earth.

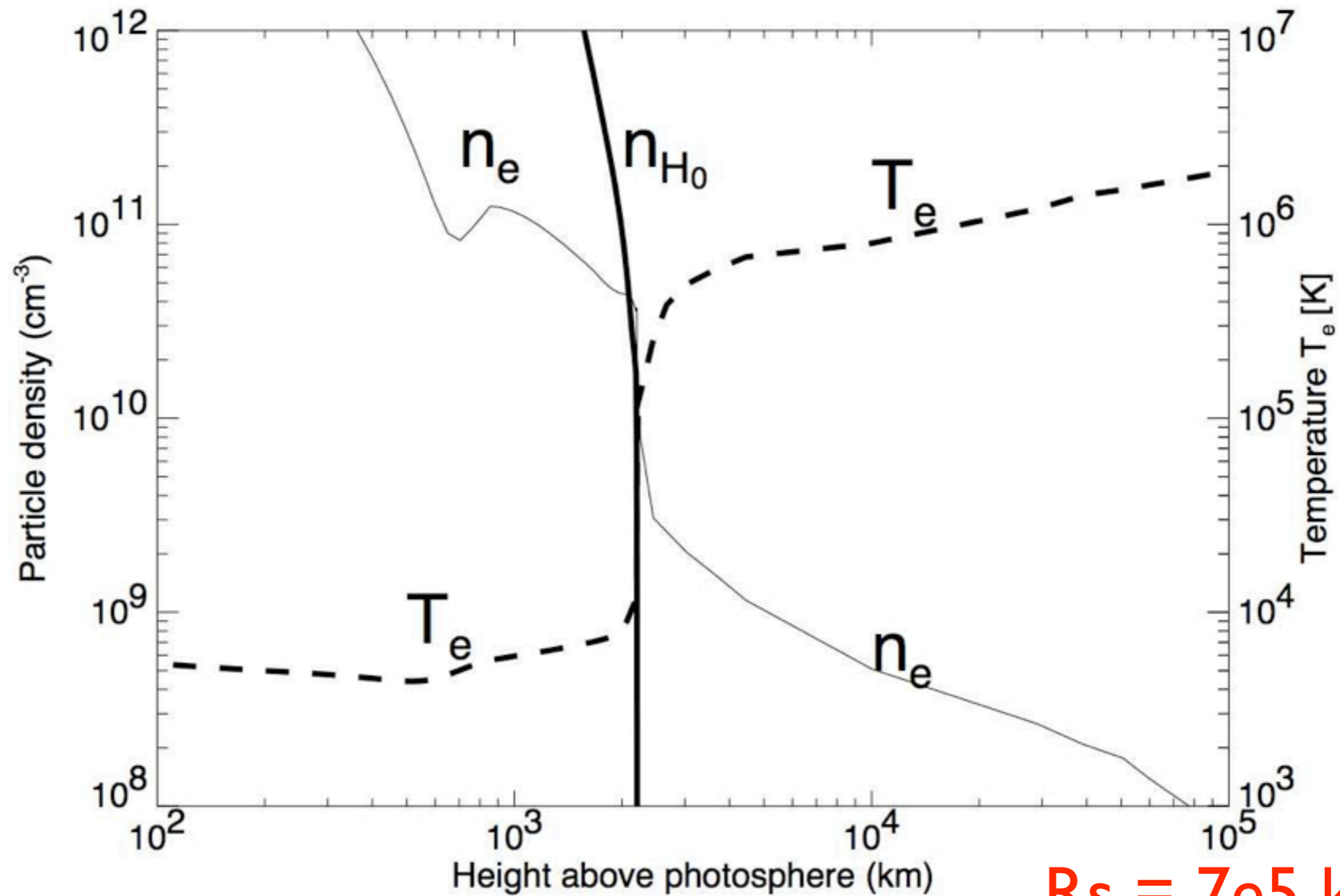
- Disabled power grids
- Destroyed satellites
- Hazards for manned space-flight
- Aurora Borealis



# Space Weather Issues

- Predict the solar wind at the Earth and interplanetary space.
- Model the initial propagation of CMEs through the corona.
- Model the initial propagation of energetic particle storms through the corona.

# 1D Model



**$R_s = 7e5$  km**

Figure 1.19: Electron density and temperature model of the chromosphere (Fontenla et al. 1990; Model FAL-C) and lower corona (Gabriel, 1976). The plasma becomes fully ionized at the sharp transition from chromospheric to coronal temperatures. In the chromosphere, the plasma is only partially ionized:  $n_e$  indicates the electron density,  $n_{H_0}$  the neutral hydrogen density.

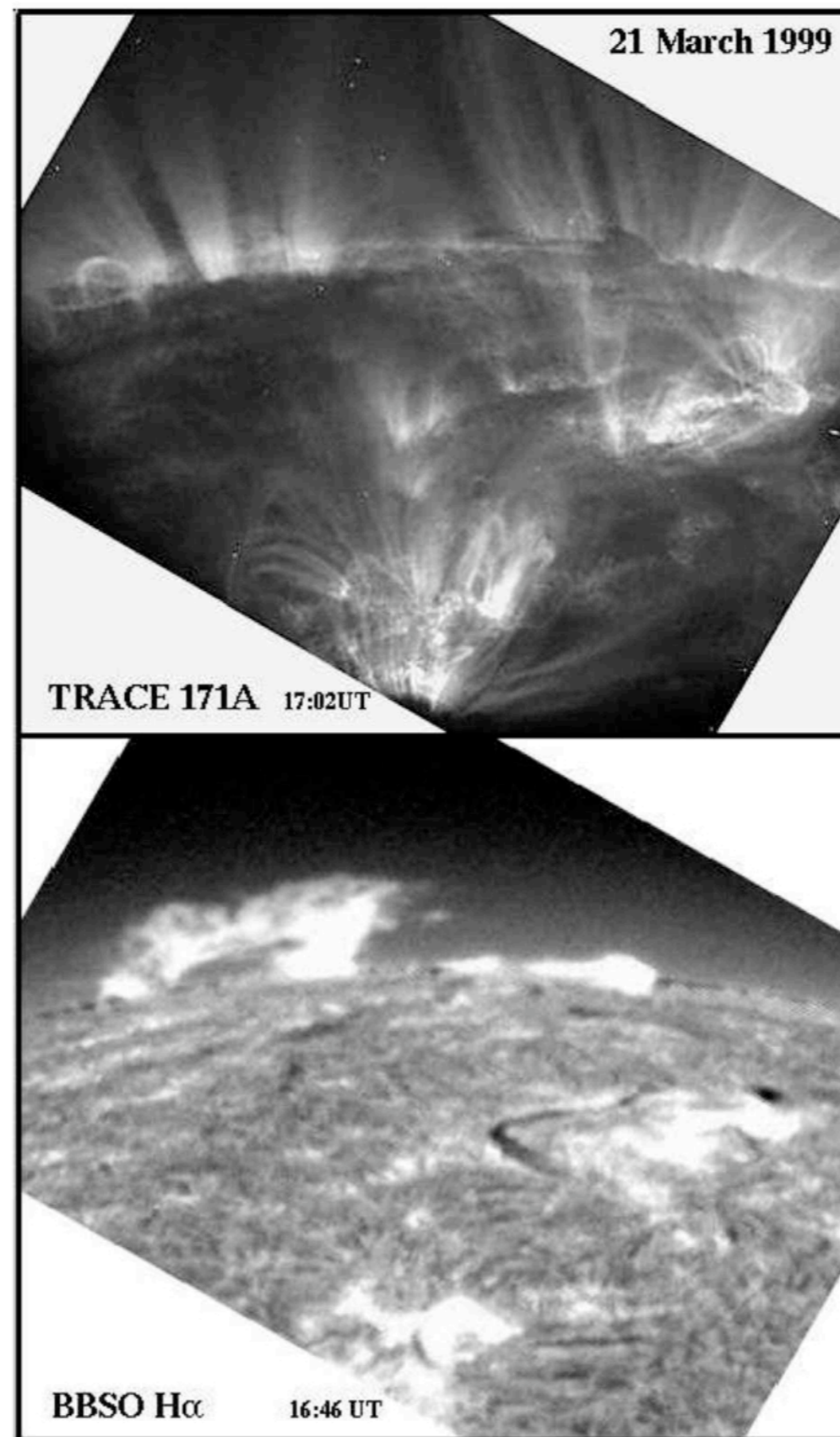


Figure 1.10: These images (taken on 1999 March 21) compare the corona seen in EUV (top panel: *TRACE*, 171 Å, T=1 MK) and the chromosphere seen in H $\alpha$  (bottom panel: *Big Bear Solar Observatory (BBSO)*, T=10,000 K). The cool filaments (on the disk) and prominences (above the limb) show up as bright structures in H $\alpha$  (bottom frame), but as dark, absorbing features in EUV (top frame) (courtesy of *TRACE* and *BBSO*).

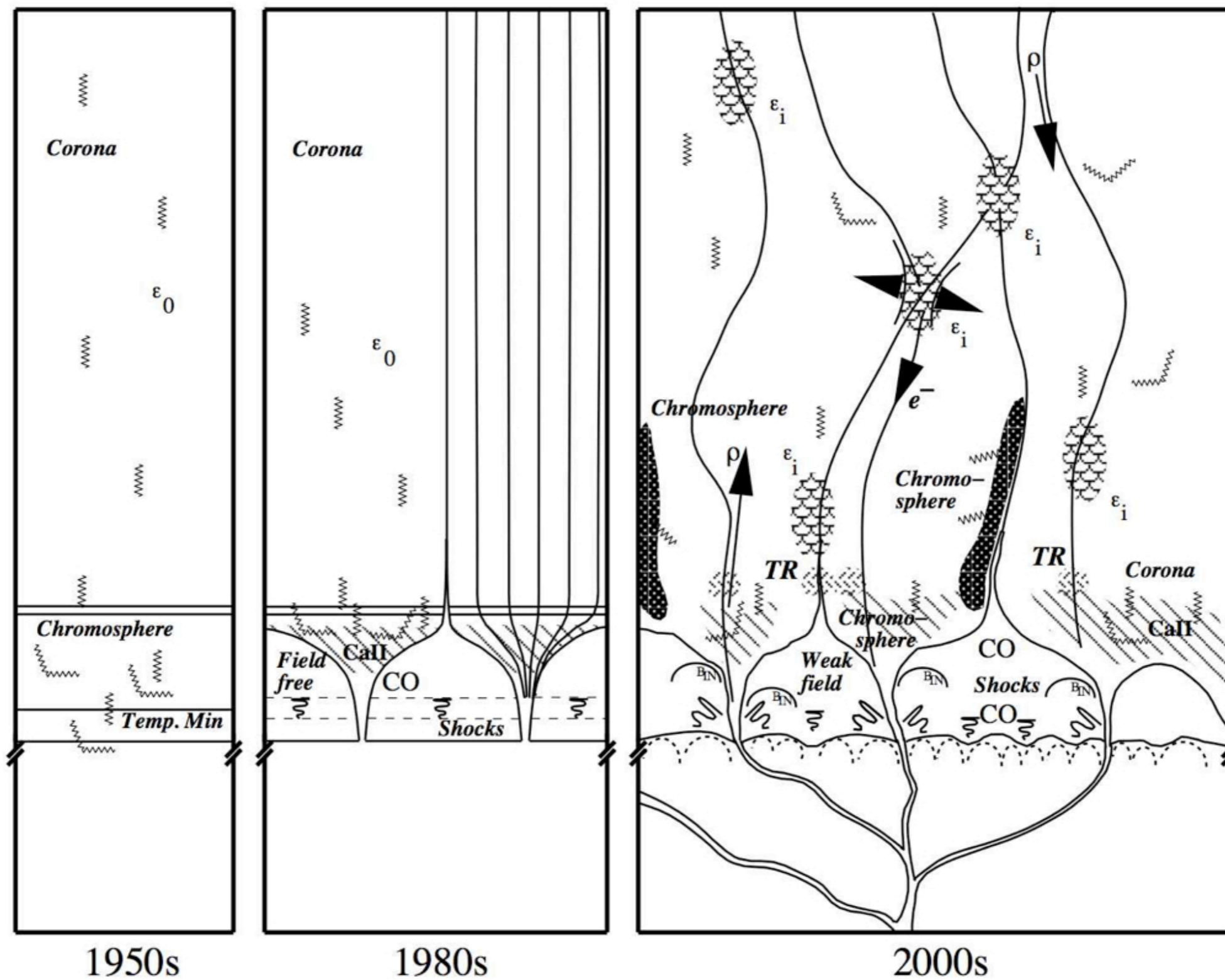


Figure 1.17: Cartoon of geometric concepts of the solar corona: gravitationally stratified layers in the 1950s (*left*), vertical fluxtubes with chromospheric canopies in the 1980s (*middle*), and a fully inhomogeneous mixing of photospheric, chromospheric, and coronal zones by dynamic processes such as heated upflows, cooling downflows, intermittent heating ( $\epsilon$ ), nonthermal electron beams ( $e^-$ ), field line motions and reconnections, emission from hot plasma, absorption and scattering in cool plasma, acoustic waves, and shocks (*right*) (Schrijver, 2001b).

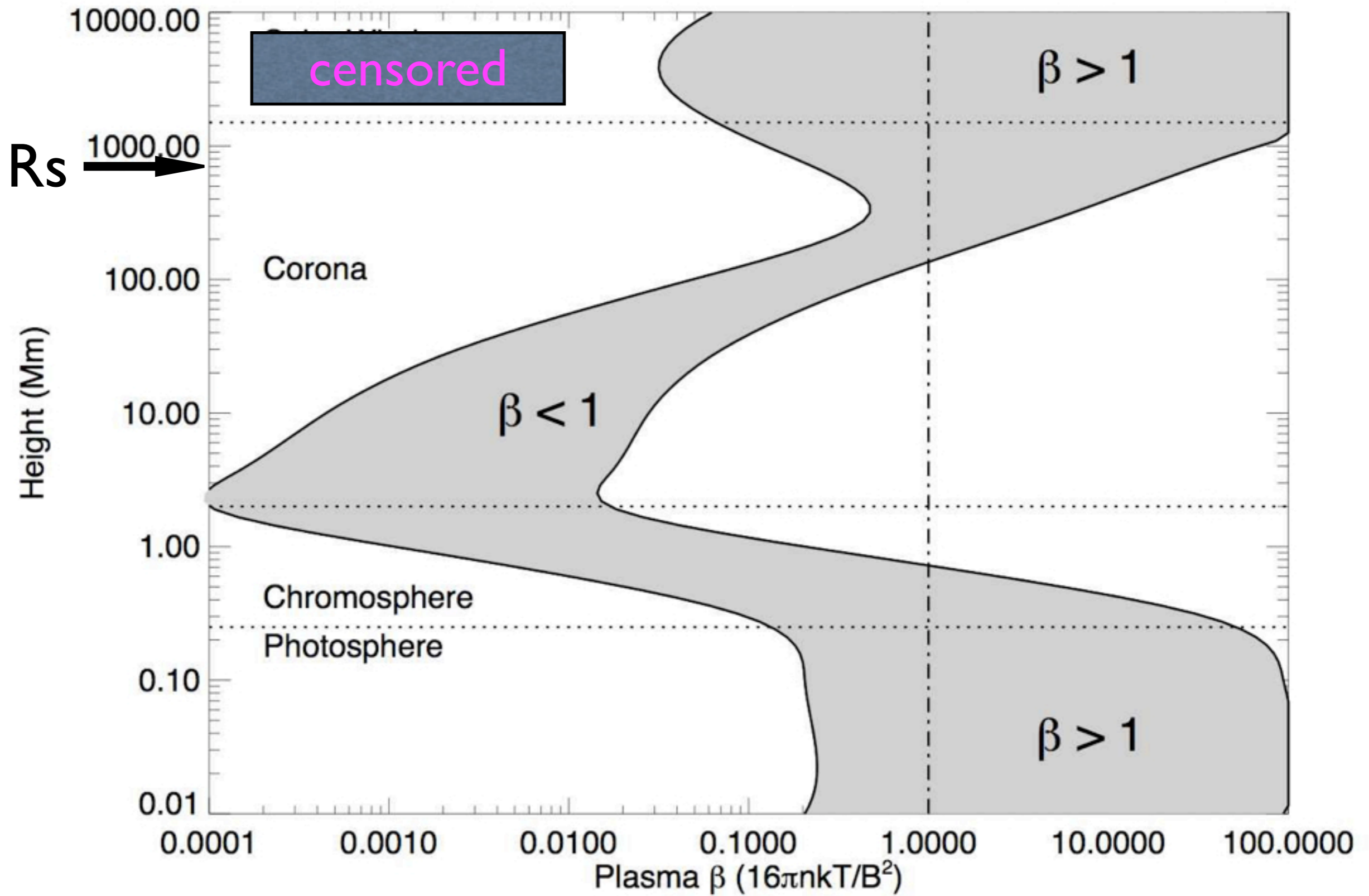
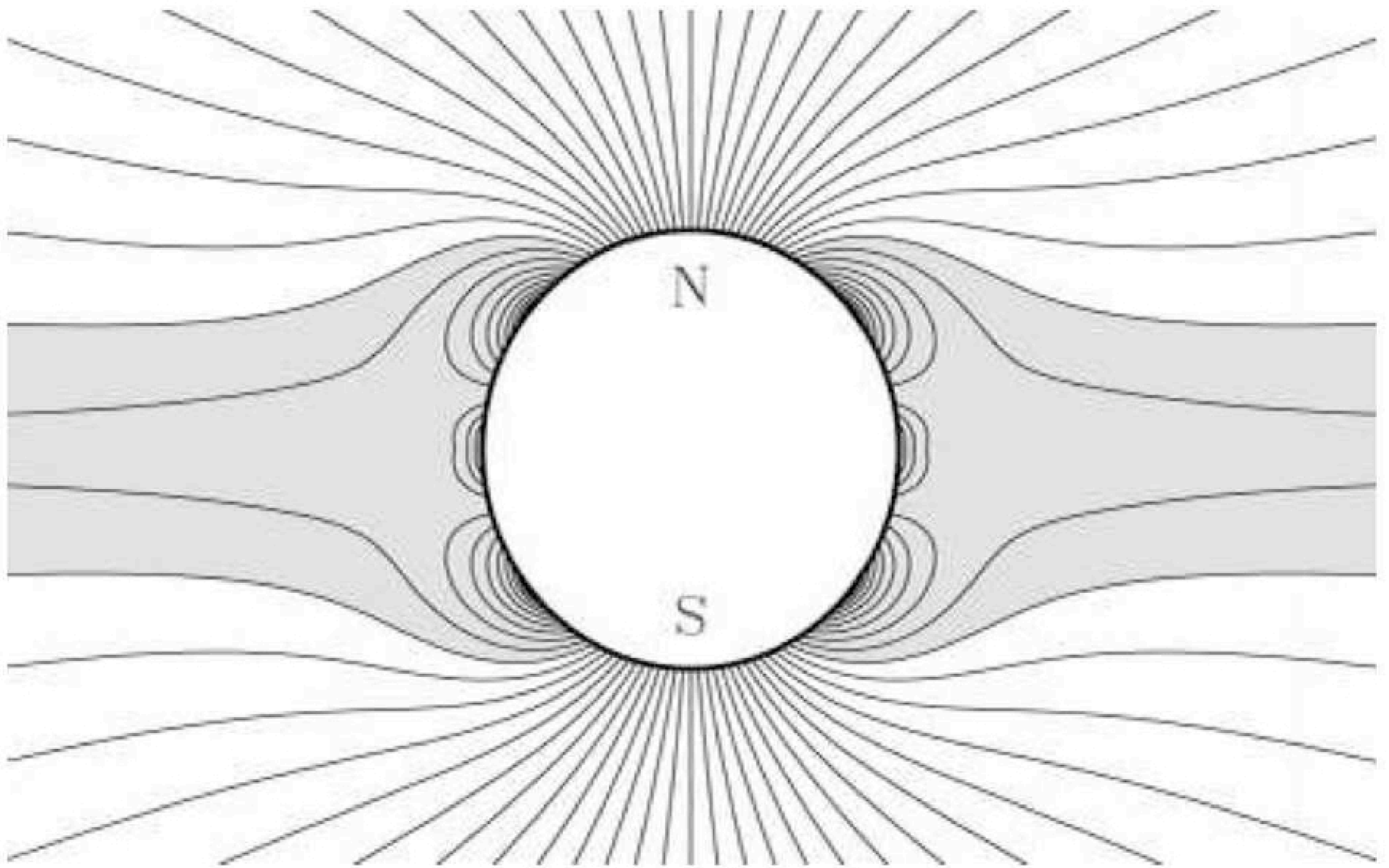


Figure 1.22: Plasma  $\beta$  in the solar atmosphere for two assumed field strengths, 100 G and 2500 G. In the inner corona ( $R \lesssim 0.2R_{\odot}$ ), magnetic pressure generally dominates static gas pressure. As with all plots of physical quantities against height, a broad spatial and temporal average is implied (Gary, 2001).



Depiction of lines of magnetic force in the semi-empirical multipol

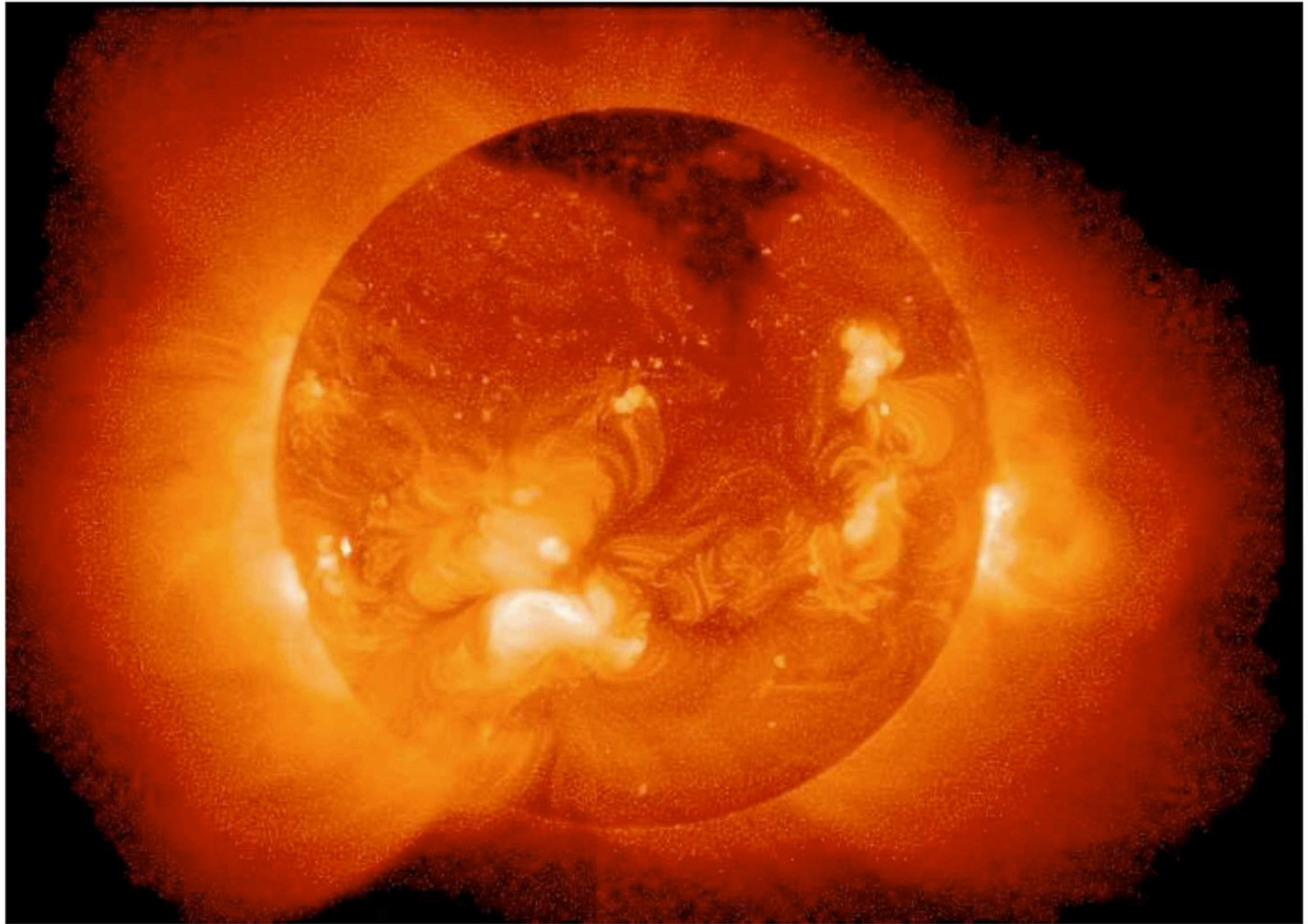


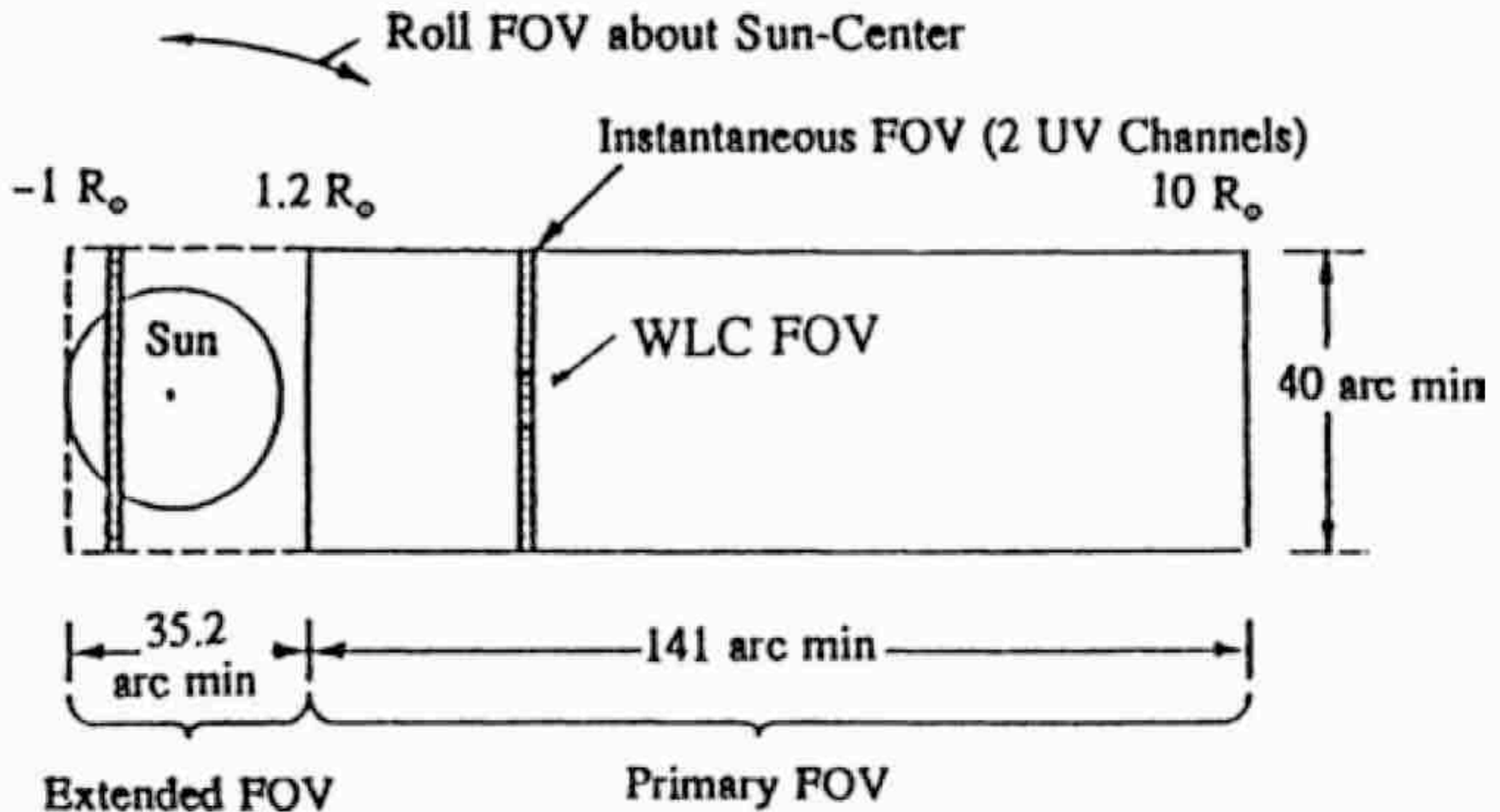
Figure 1.8: Soft X-ray image of the extended solar corona recorded on 1992 August 26 by the *Yohkoh* Soft X-ray Telescope (SXT). The image was made up from two pointings of the spacecraft, one to the east and one to the west, to capture the distant corona far above the Sun's limb (courtesy of *Yohkoh* Team).

# key UV spectral observations above 1.5 Rs from UVCS

- H Ly-alpha line (pure resonant scattering of disk radiation)
- O5+ 103.2, 103.7 nm doublet (collisional emission + resonant scattering)



# The UltraViolet Coronagraph Spectrometer (UVCS) FOV



The field of view of UVCS/SOHO. From Kohl et al. (1995a)

# UVCS grating

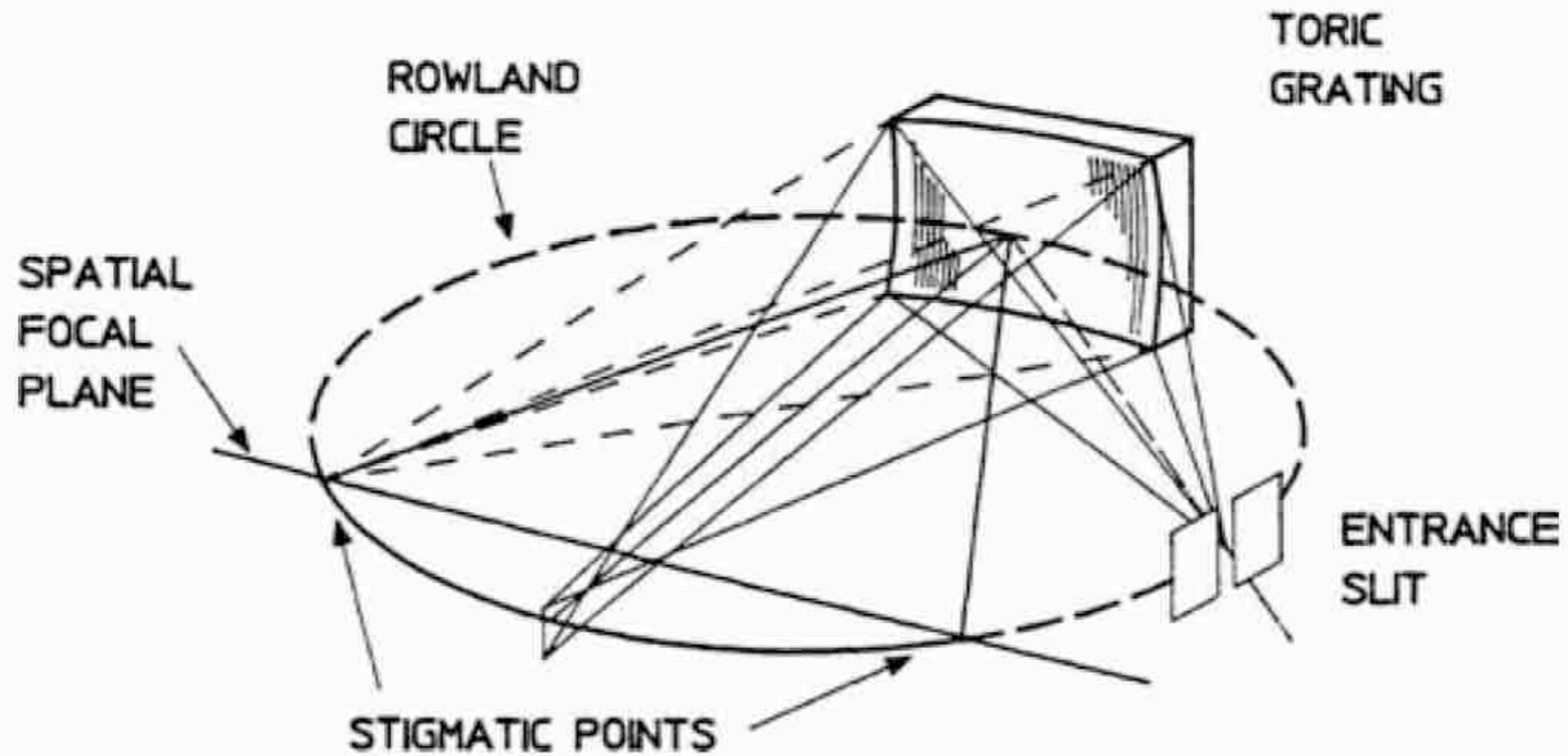


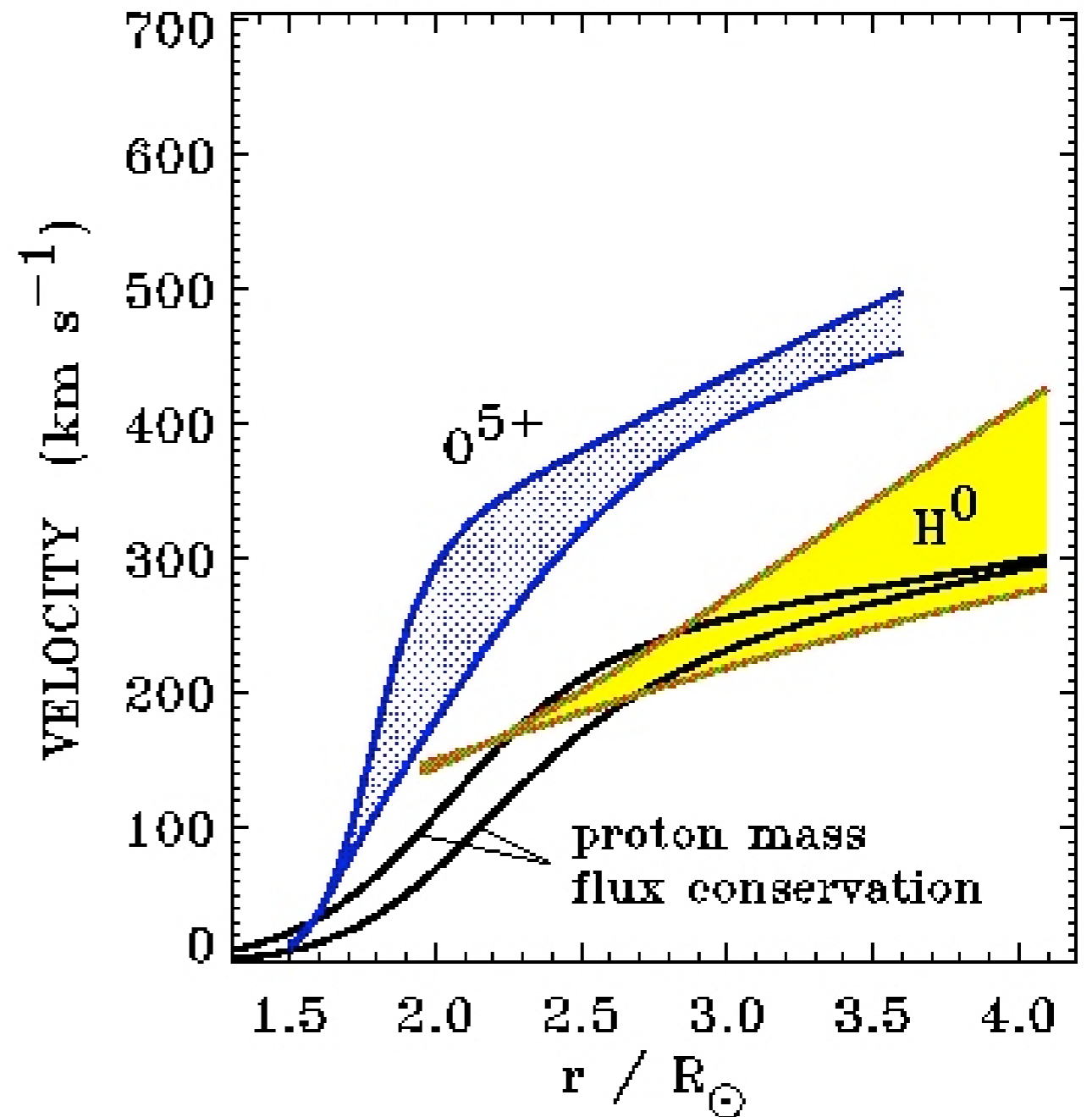
**Fig. 11** Isometric display of the imaging properties between the two stigmatic points of the UVCS/SOHO spectrometer

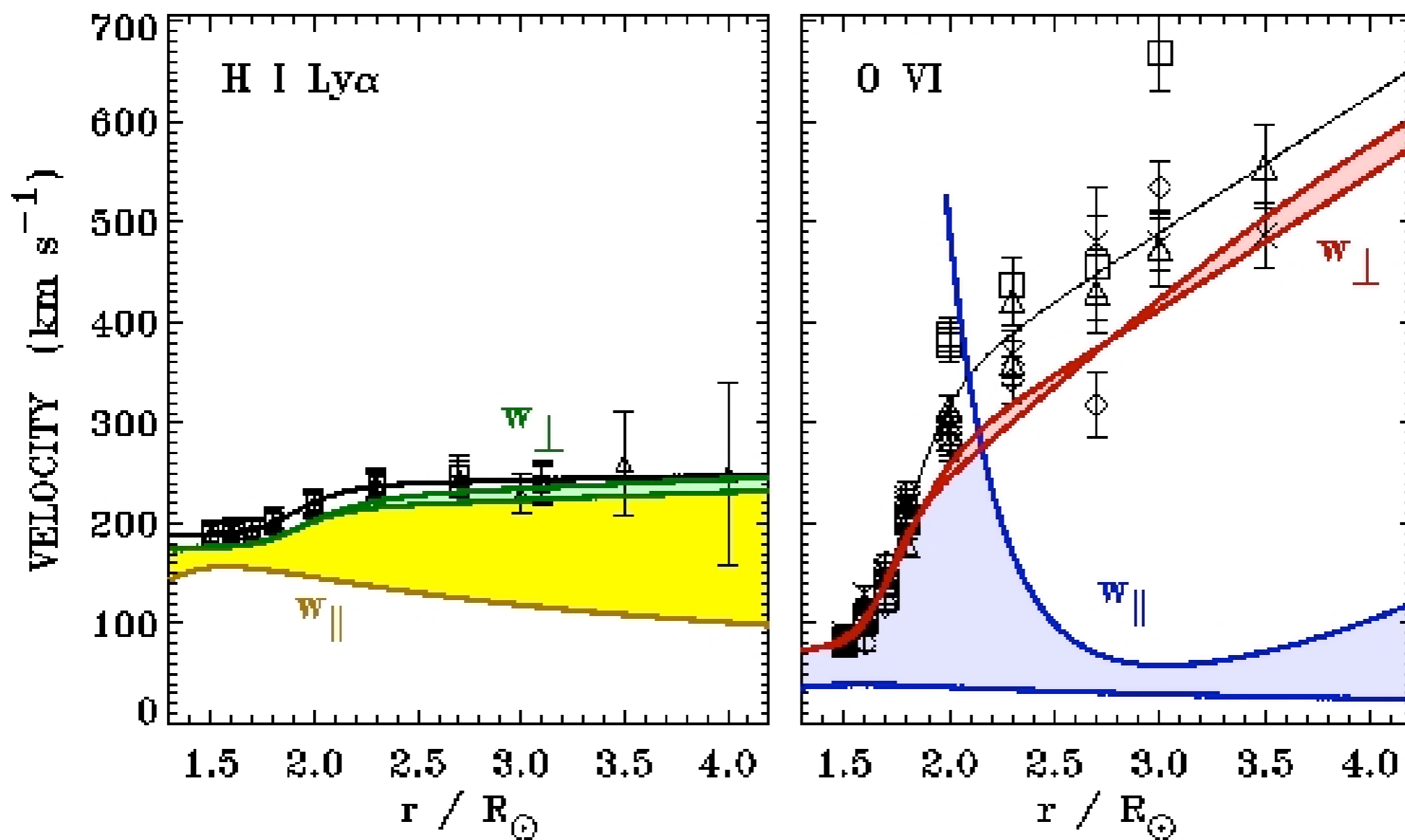
# UVCS Results

Empirically derived particle outflow speeds over the solar poles in late 1996 and early 1997. The yellow region denotes the range of hydrogen speeds able to reproduce observational data from UVCS, and the blue region denotes the corresponding range of speeds for ionized oxygen ( $O^{5+}$ ). The black lines denote the proton outflow speed derived from mass flux conservation: for a time-steady flow, the product of the density, speed, and flow-tube area should be constant, and we use density and polar flow-tube information, as well as in-situ mass flux data from Ulysses, to define the constant.

(Kohl et al. 1998, *Astrophys. J.*, 501, L127;  
Cranmer et al. 1999, *Astrophys. J.*, 511, 481)

## Outflow velocities:





Line widths and empirical most-probable speeds for neutral hydrogen (H) and ionized oxygen ( $\text{O}^{5+}$ ) derived from emission line profiles measured with UVCS above polar coronal holes in late 1996 and early 1997. The symbols with error bars denote the observed half-widths of the lines (in Doppler velocity units) as a function of heliocentric distance, and the thin black lines are a fit to these values. The derived ranges of most-probable speeds ( $w$ ) are plotted as filled regions bounded by thick lines. For hydrogen, the uncertainty range of the speeds parallel to the radial magnetic field (yellow) extend up to the speeds in the perpendicular direction (green).

# 3D (and higher) Structure Determination via Tomographic Reconstruction

# Dedicated Sun-observing satellites:

SOHO (launched 1995; operational)

TRACE (launched 1998; operational)

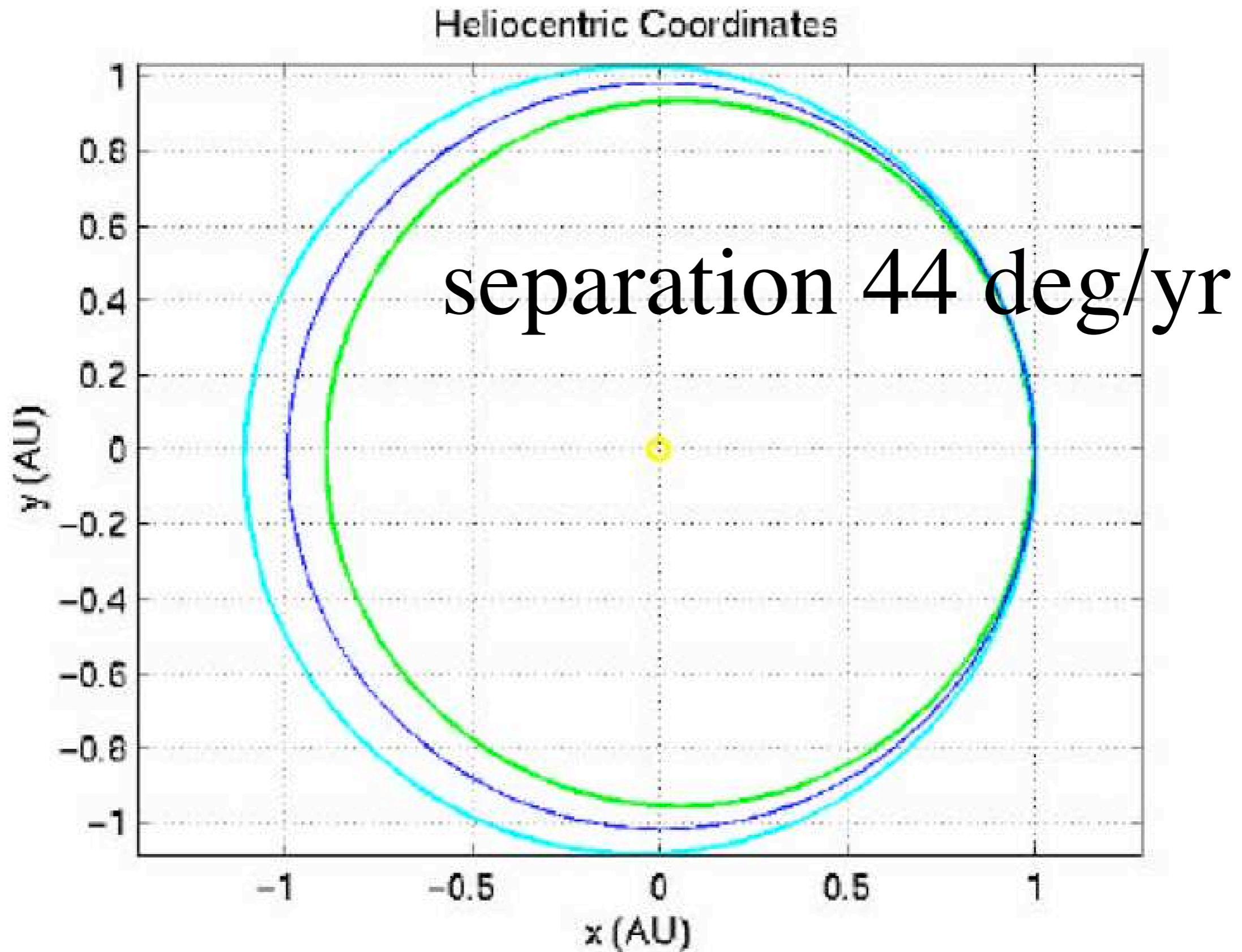
RHESSI (launched 2002; operational)

STEREO (spring 2006) - **dual spacecraft!!!**

Solar-B (fall 2006)

SDO (2008)

# STEREO orbits:



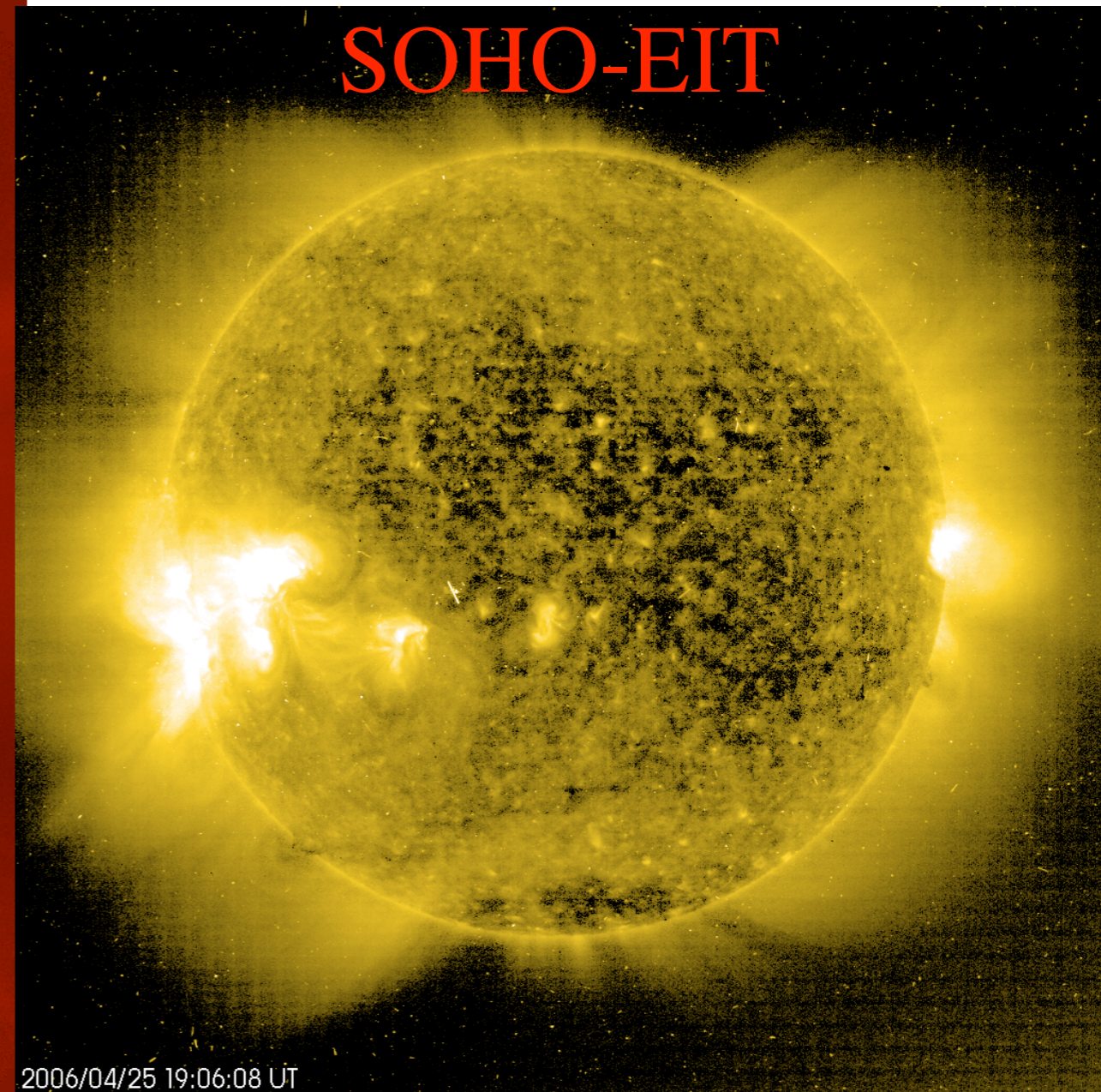
White-light and Extreme Ultraviolet (EUV) imagers see the solar corona in projection.

SOHO-LASCO



WL image

SOHO-EIT



EUV image



The white-light image intensities are related to the corona's electron number density via a line-of-sight (LOS) integral.

$$I_k = \int_{\text{LOS}} dl w(\vec{\rho}_k, l\vec{q}) N_e(\vec{\rho}_k + l\vec{q})$$



pixel  
intensity



weight  
function



electron  
density

The synodic solar rotation period is about 28 days and it takes 14 days to obtain enough angular coverage for tomographic inversion. This can be treated as a discrete linear inversion problem.

$$\vec{y} = A\vec{x} + \vec{\gamma}$$

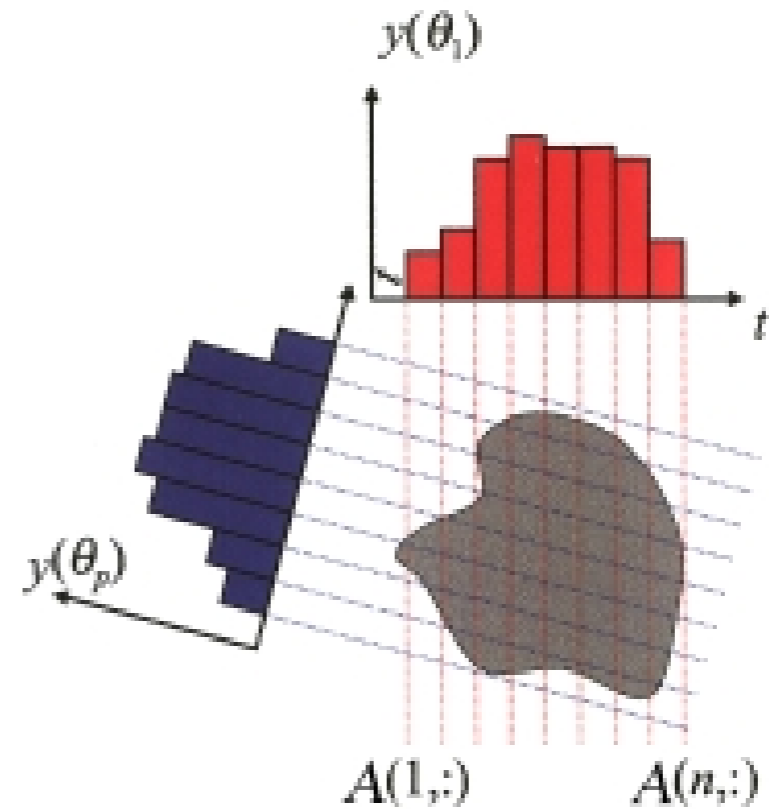
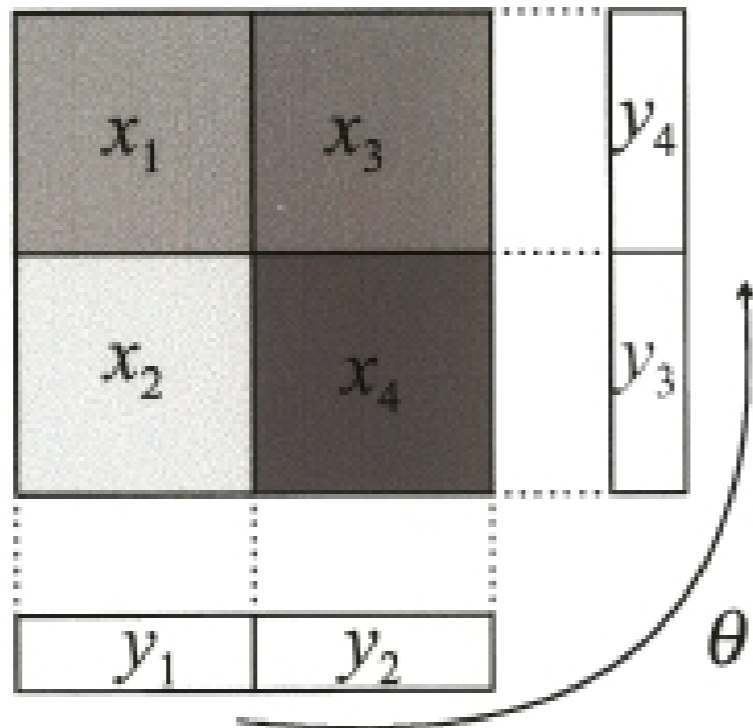
The diagram illustrates the linear inversion equation  $\vec{y} = A\vec{x} + \vec{\gamma}$ . Three blue arrows point from labels below to terms in the equation: one from 'intensity vector' to  $\vec{y}$ , one from 'electron density' to  $\vec{x}$ , and one from 'noise' to  $\vec{\gamma}$ . The matrix  $A$  is not labeled with an arrow.

intensity  
vector

electron  
density

noise

SRT takes advantage of the different view angles provided by solar rotation to determine  $N_e$ .

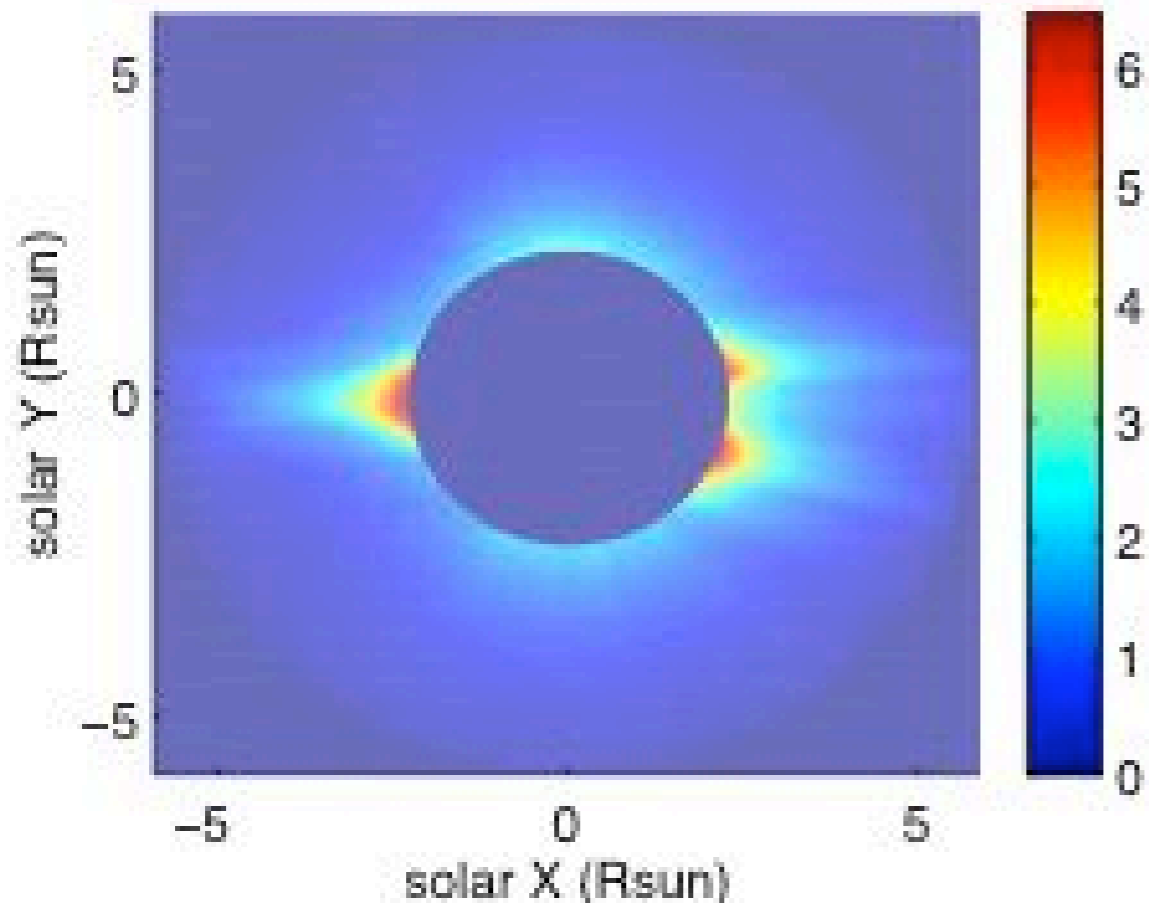


$$\begin{pmatrix} y_1 \\ y_2 \\ y_3 \\ y_4 \end{pmatrix} = \begin{bmatrix} 1 & 1 & 0 & 0 \\ 0 & 0 & 1 & 1 \\ 0 & 1 & 0 & 1 \\ 1 & 0 & 1 & 0 \end{bmatrix} \begin{pmatrix} x_1 \\ x_2 \\ x_3 \\ x_4 \end{pmatrix} \iff \mathbf{y} = \mathbf{A}\mathbf{x}$$

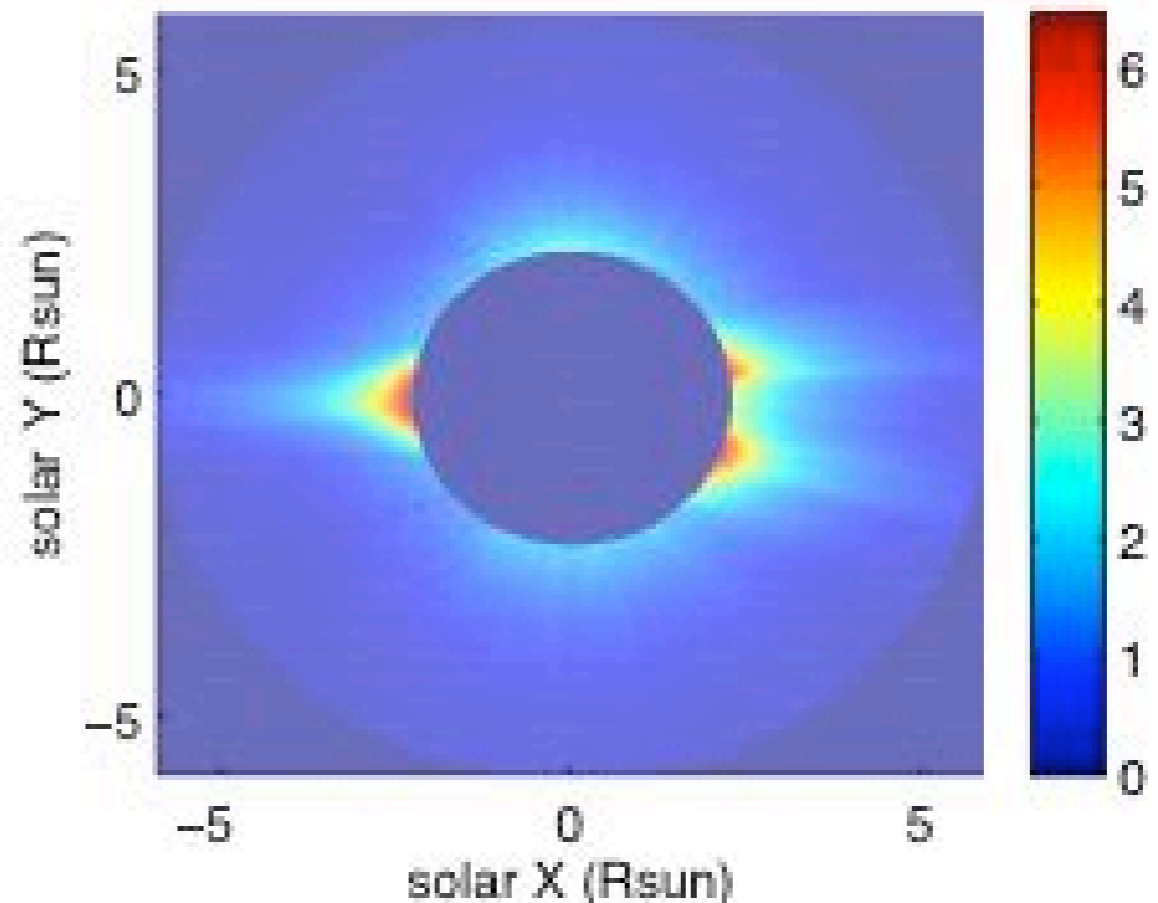
# LASCO-C2 Reconstructions

Reconstructions were performed using  $\rho_B$  data from the Aug 1996, near solar minimum. These reconstructions used 13 input images take about 24 hr apart.

Synthetic Image (output)

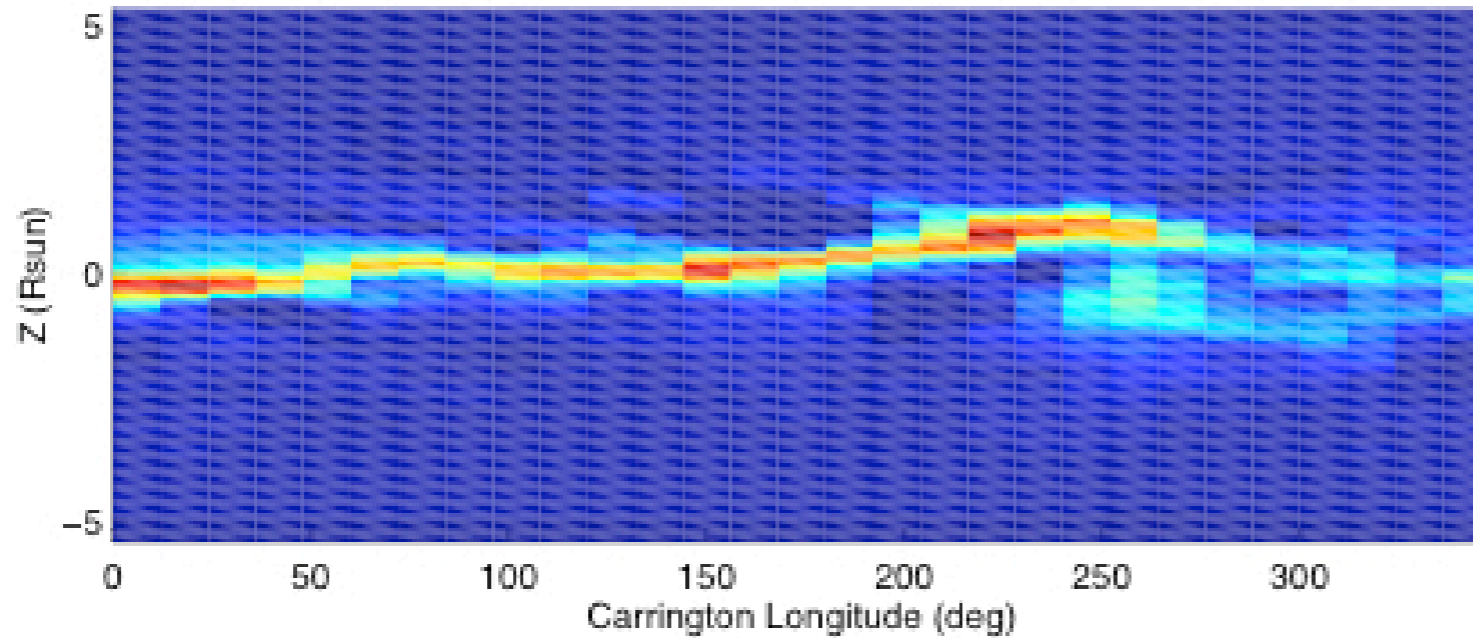


LASCO-C2 Image (input)

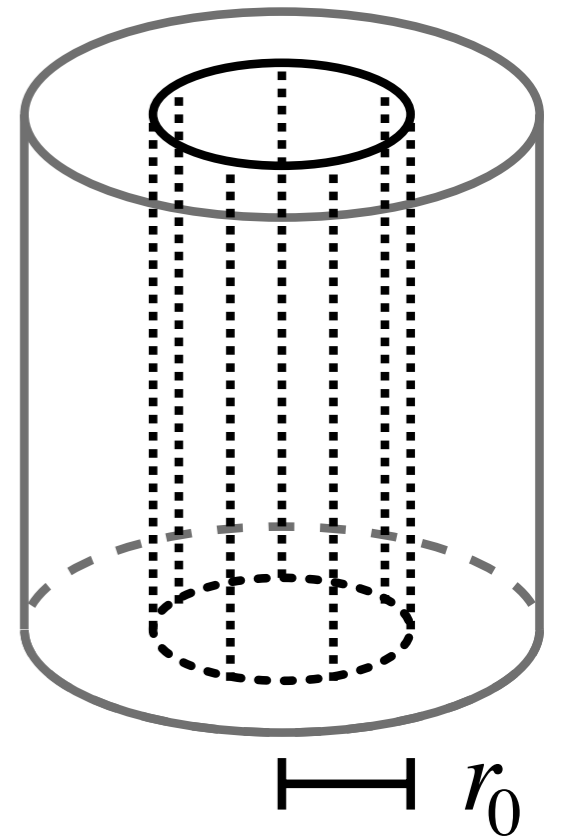
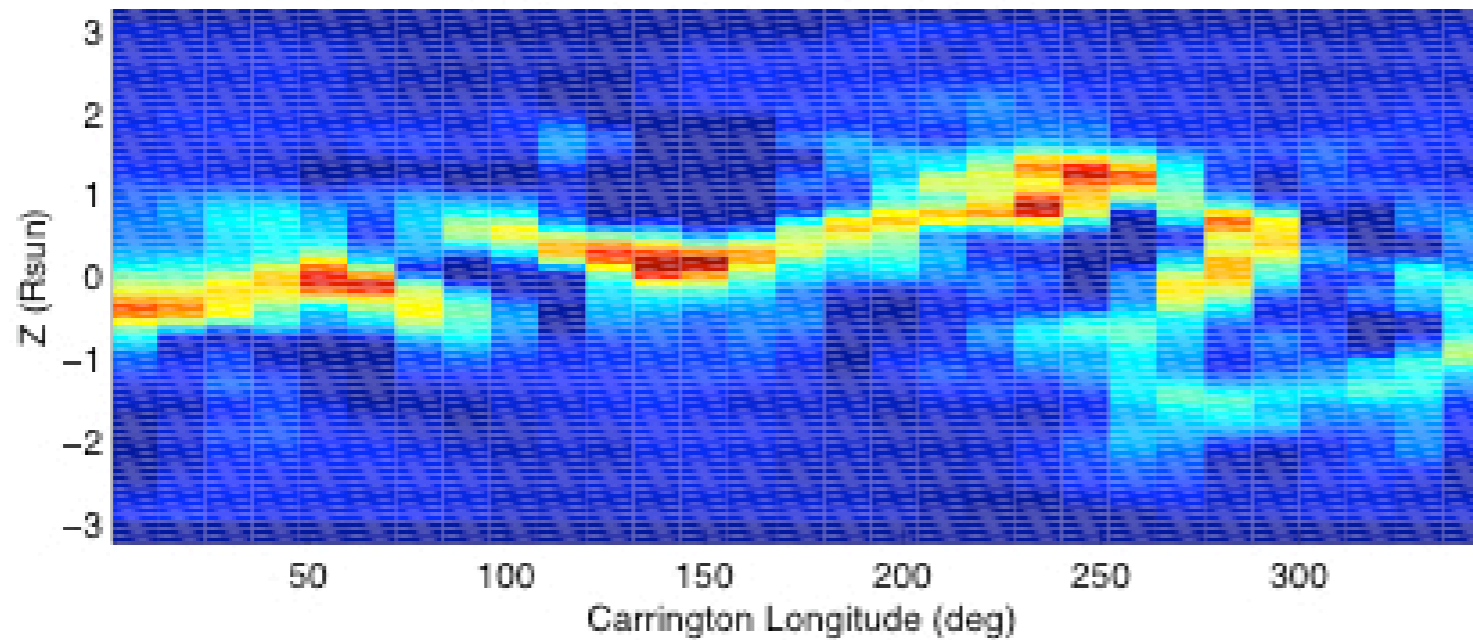


# Cylindrical Shell Cuts from Reconstruction:

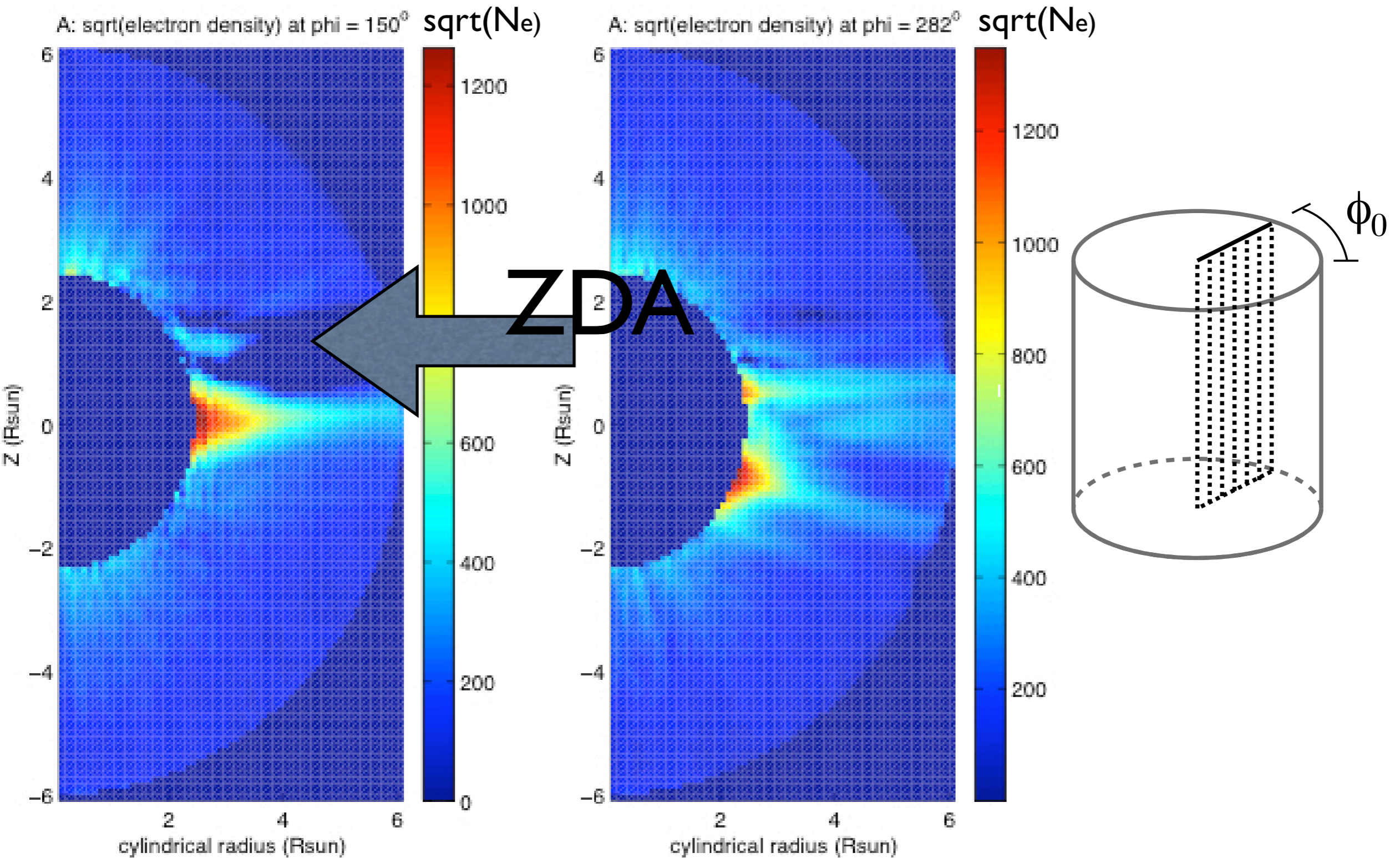
A: coronal electron density at  $\rho = 3.3359 R_{\text{sun}}$



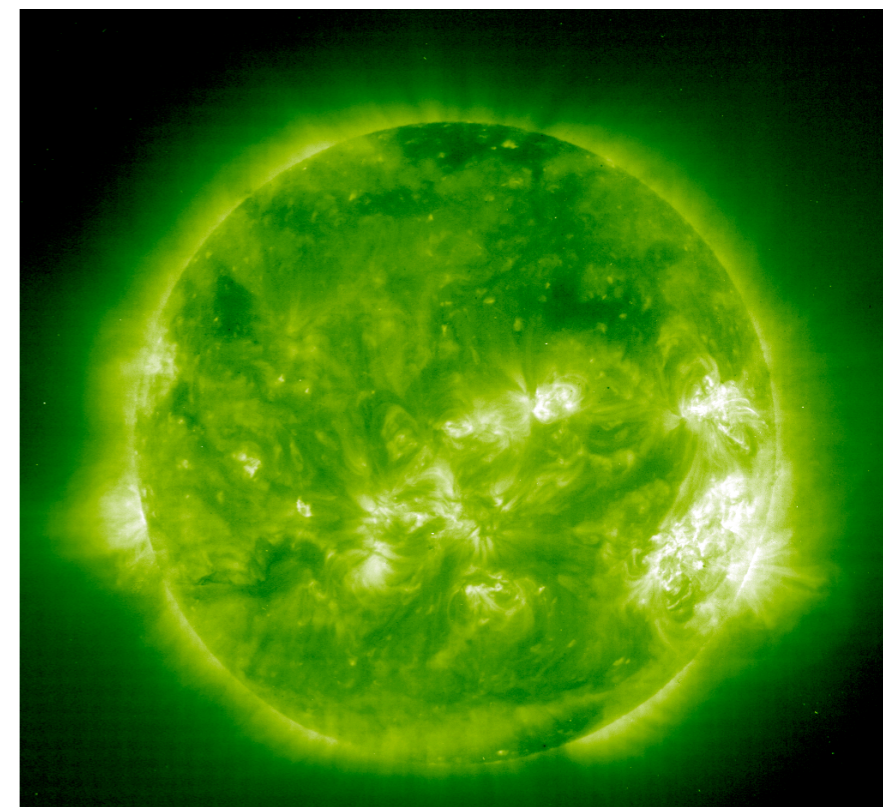
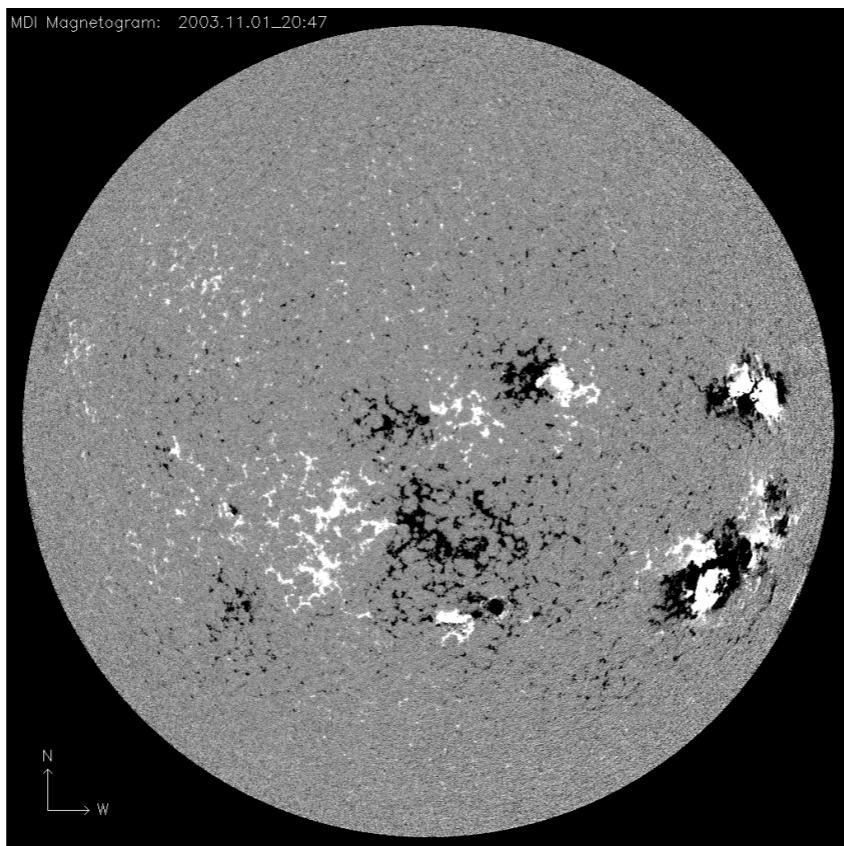
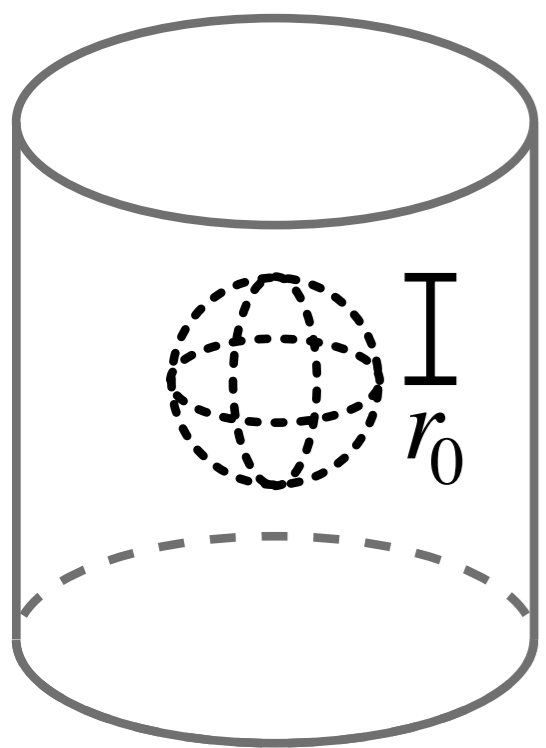
A: coronal electron density at  $\rho = 5.2422 R_{\text{sun}}$



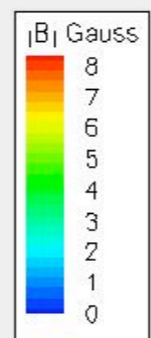
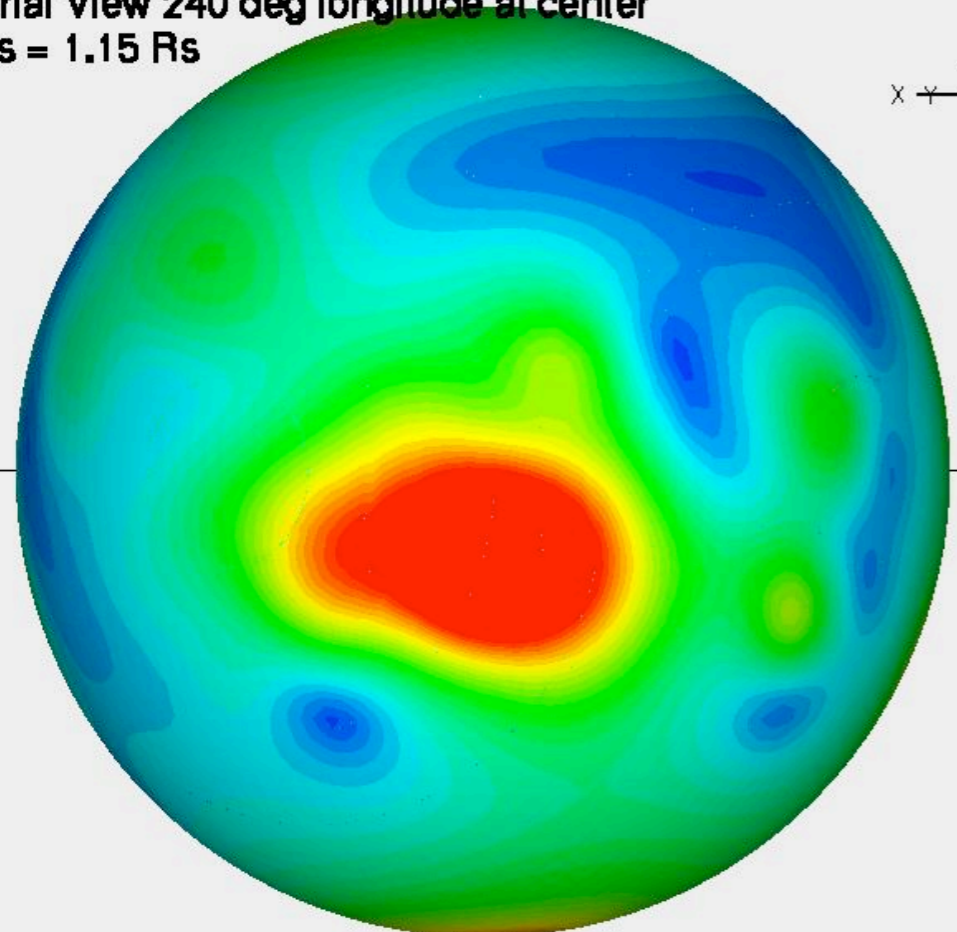
# Radial Cuts from Reconstruction:



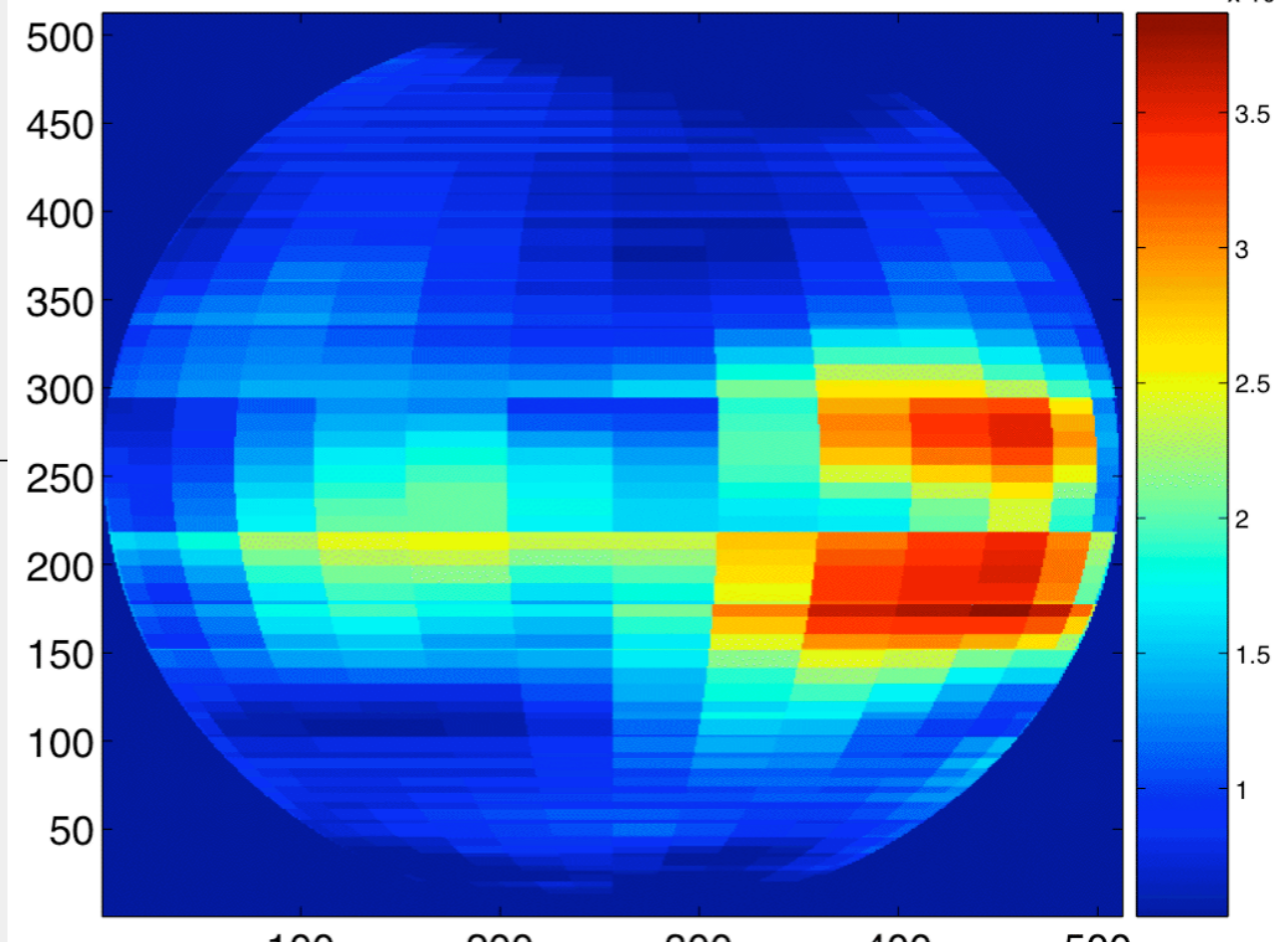
# Equatorial View (240 deg) 1.15 Rs



Equatorial View 240 deg longitude at center  
Radius = 1.15 Rs



Equatorial view: N. at top, center is 240 deg longitude,  $r_0=1.15$



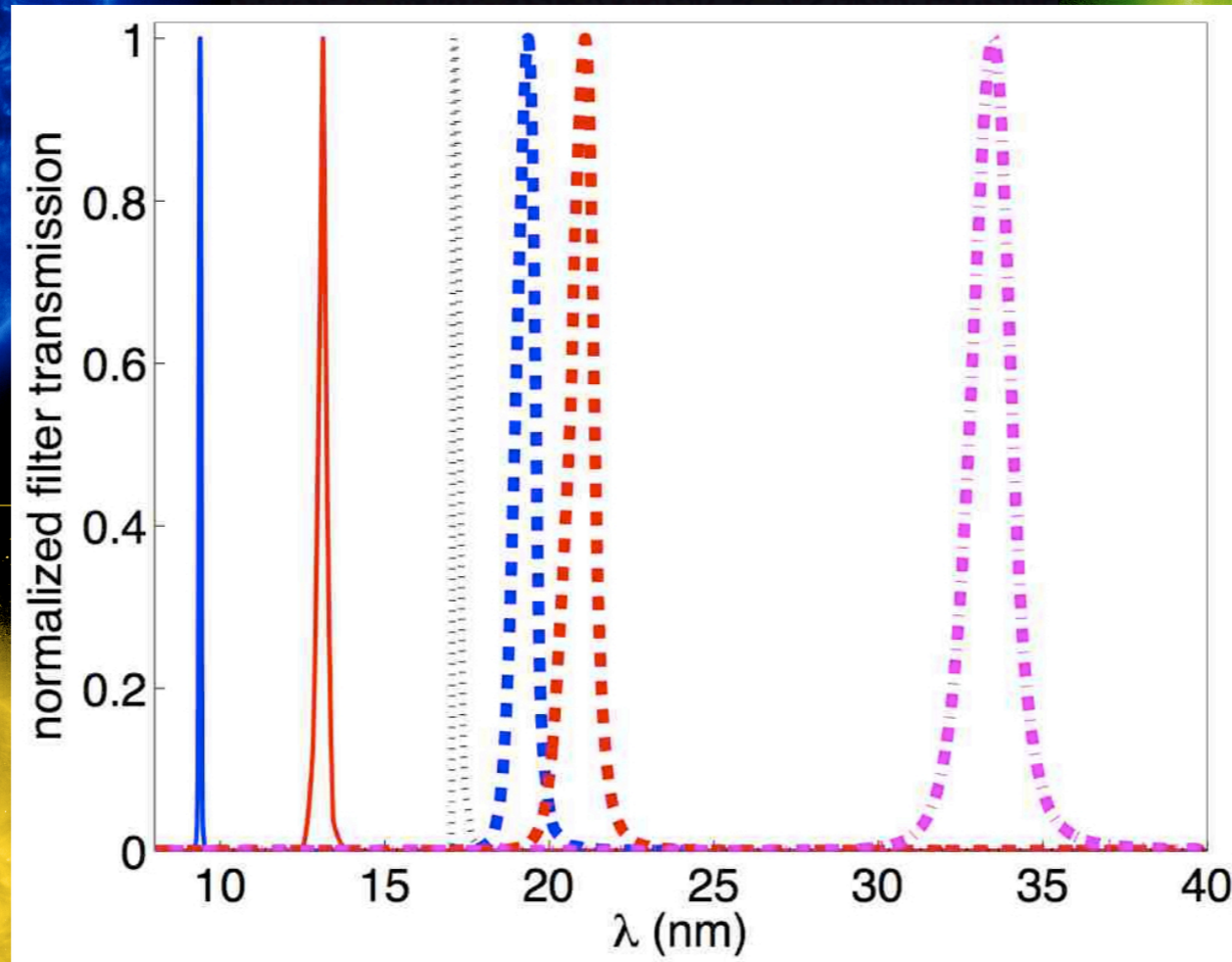
3D Te distribution  
determination via EUV  
Rotational Tomography  
(DEMT)



# Input: multi-band EUV images

17.1 nm

19.5 nm



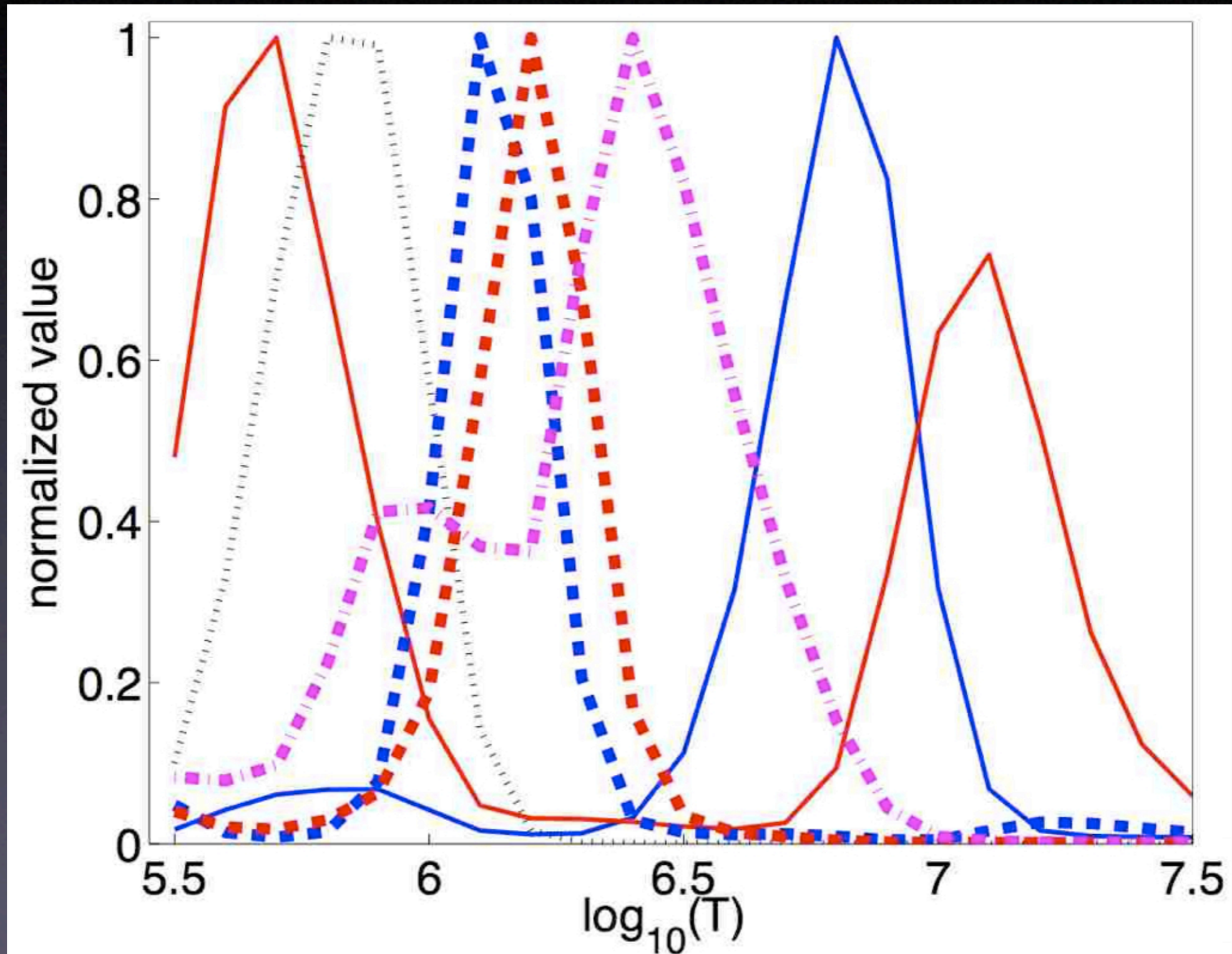
28.4 nm

30.4 nm

2006/02/25 19:00:13 UT

2006/02/25 19:06:07 UT

Each band has a different temperature sensitivity (plasma emission model).



Thus, each pixel of an EUV image sees the contributions from plasma parcels at different temperatures along its line-of-sight.

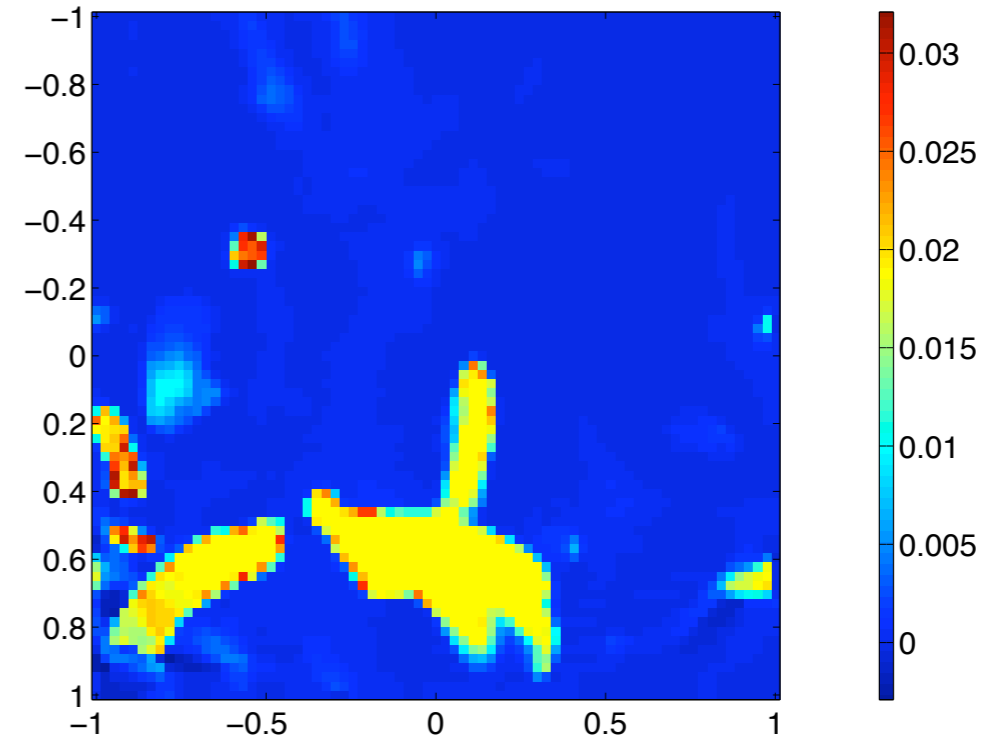
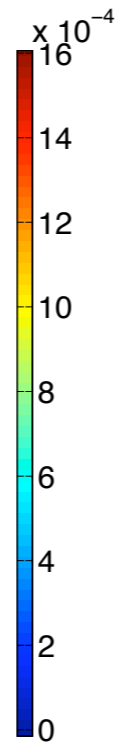
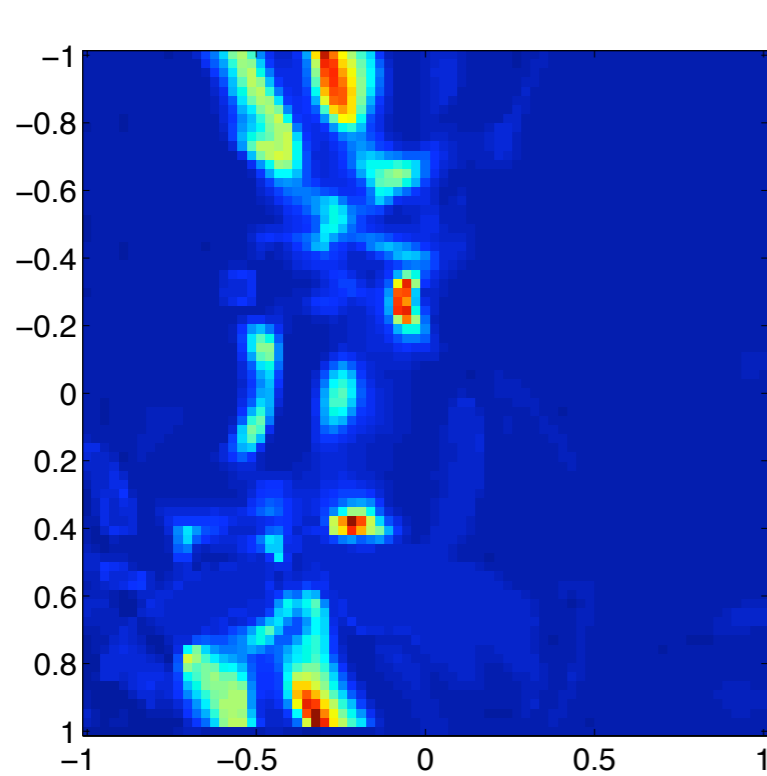
One may determine  $T$  at each point by a two step process:

- 1) Spatial tomography in each band
- 2) Temperature inversion in each voxel

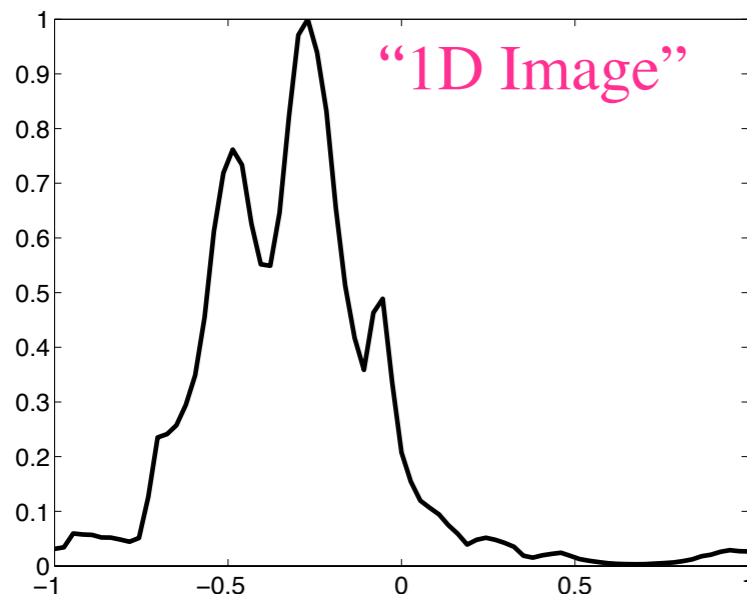
# Simulation:

Fe XVIII (94 Å)

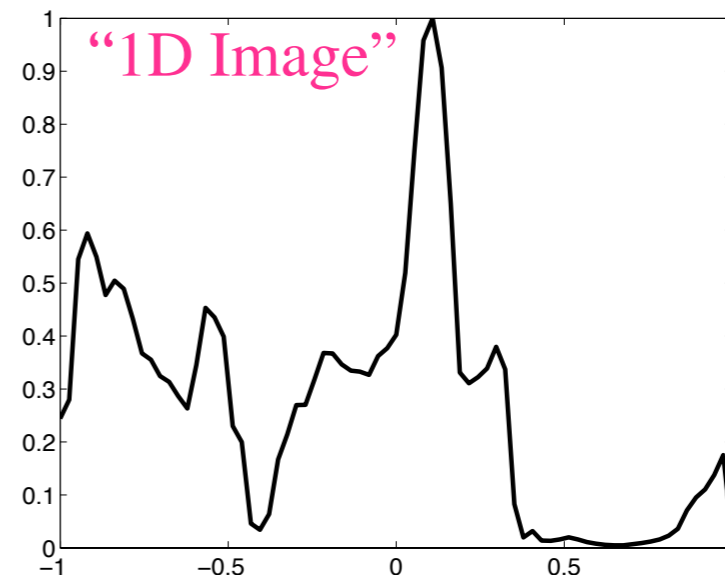
Fe VII, XX, XXIII (131 Å)



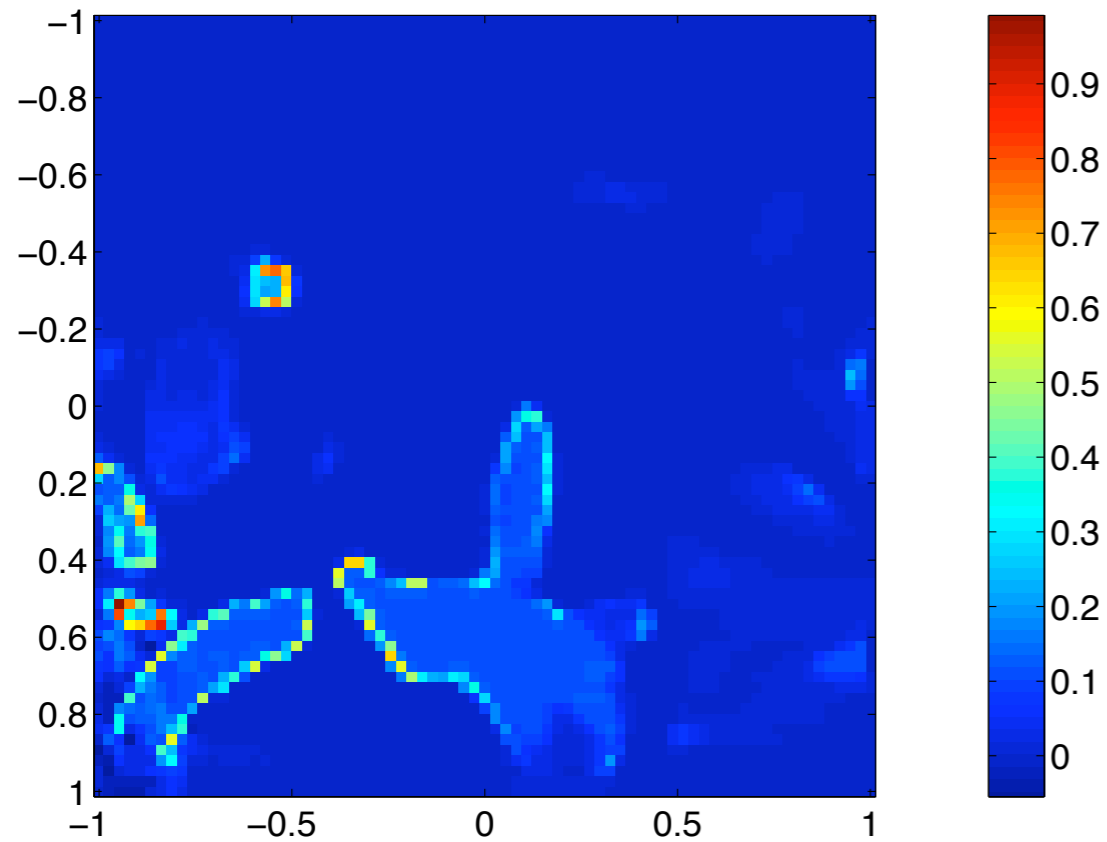
Vertical LOS Projections



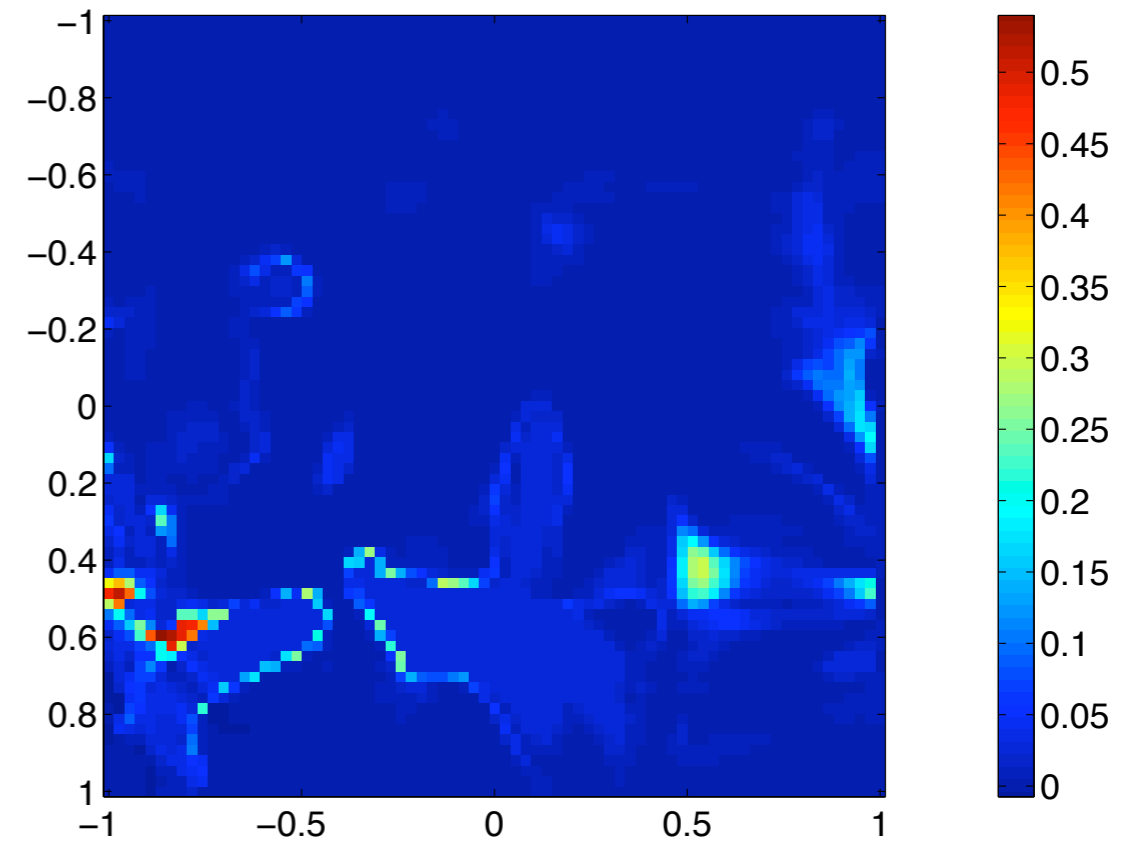
(54 such projections were used for each bandpass)



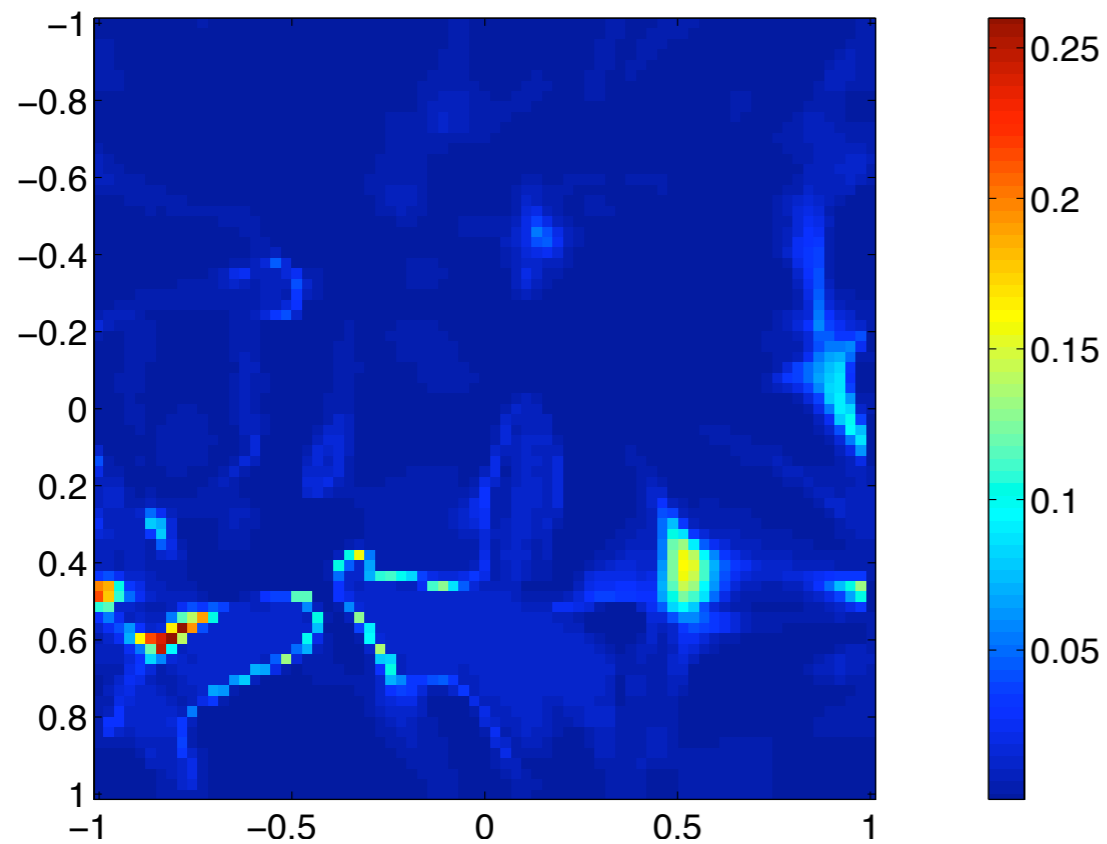
# Fe IX (171 Å)



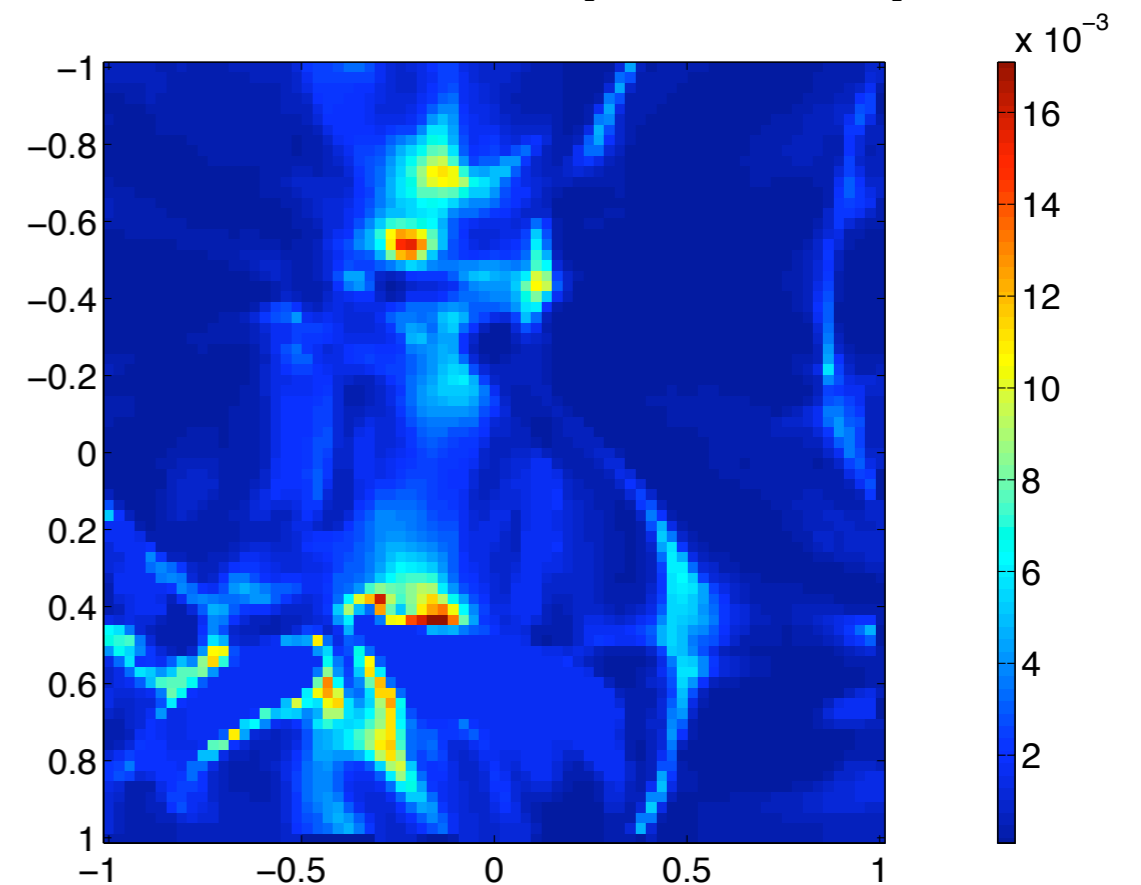
# Fe XII, XXIV (194 Å)



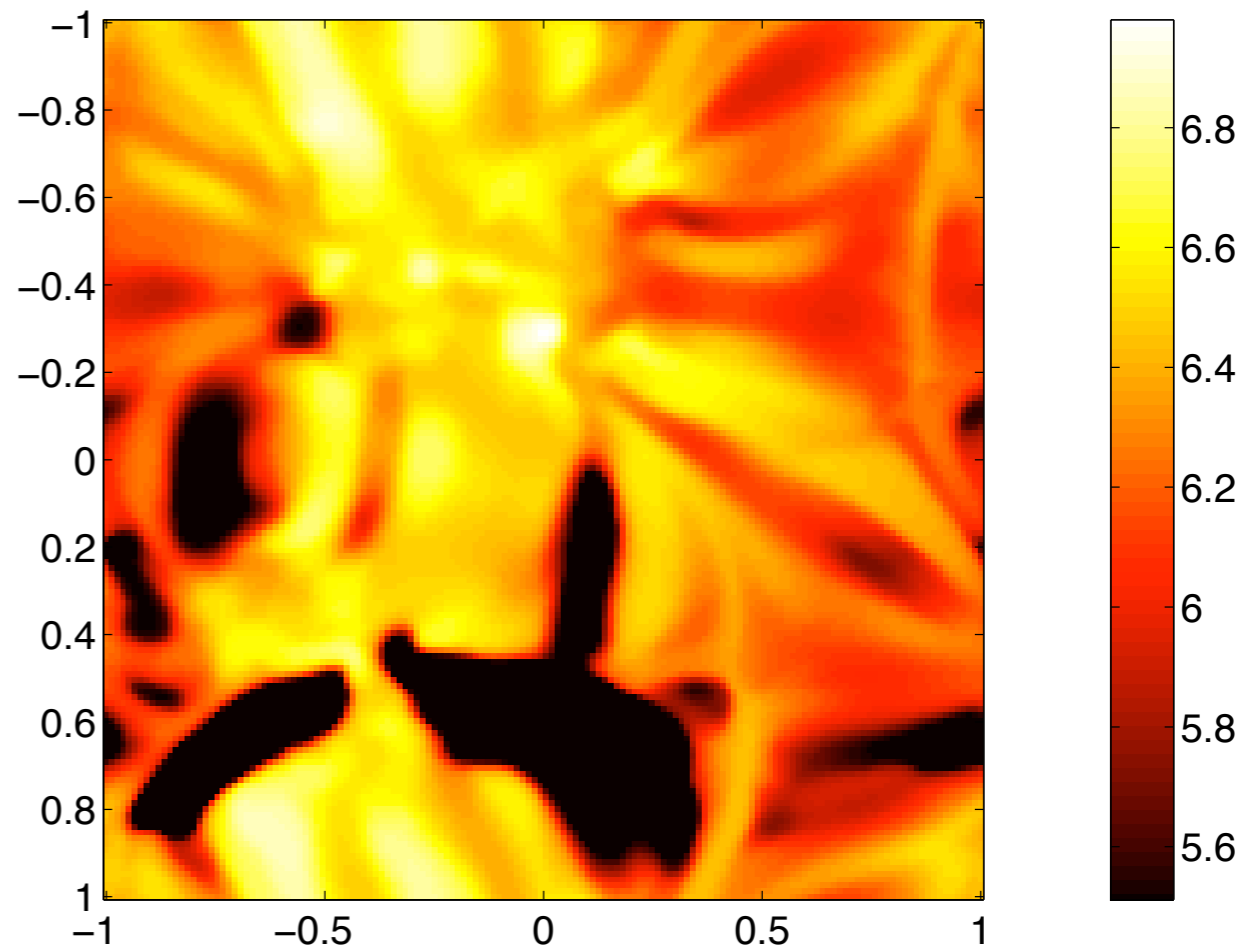
# Fe XIV (211 Å)



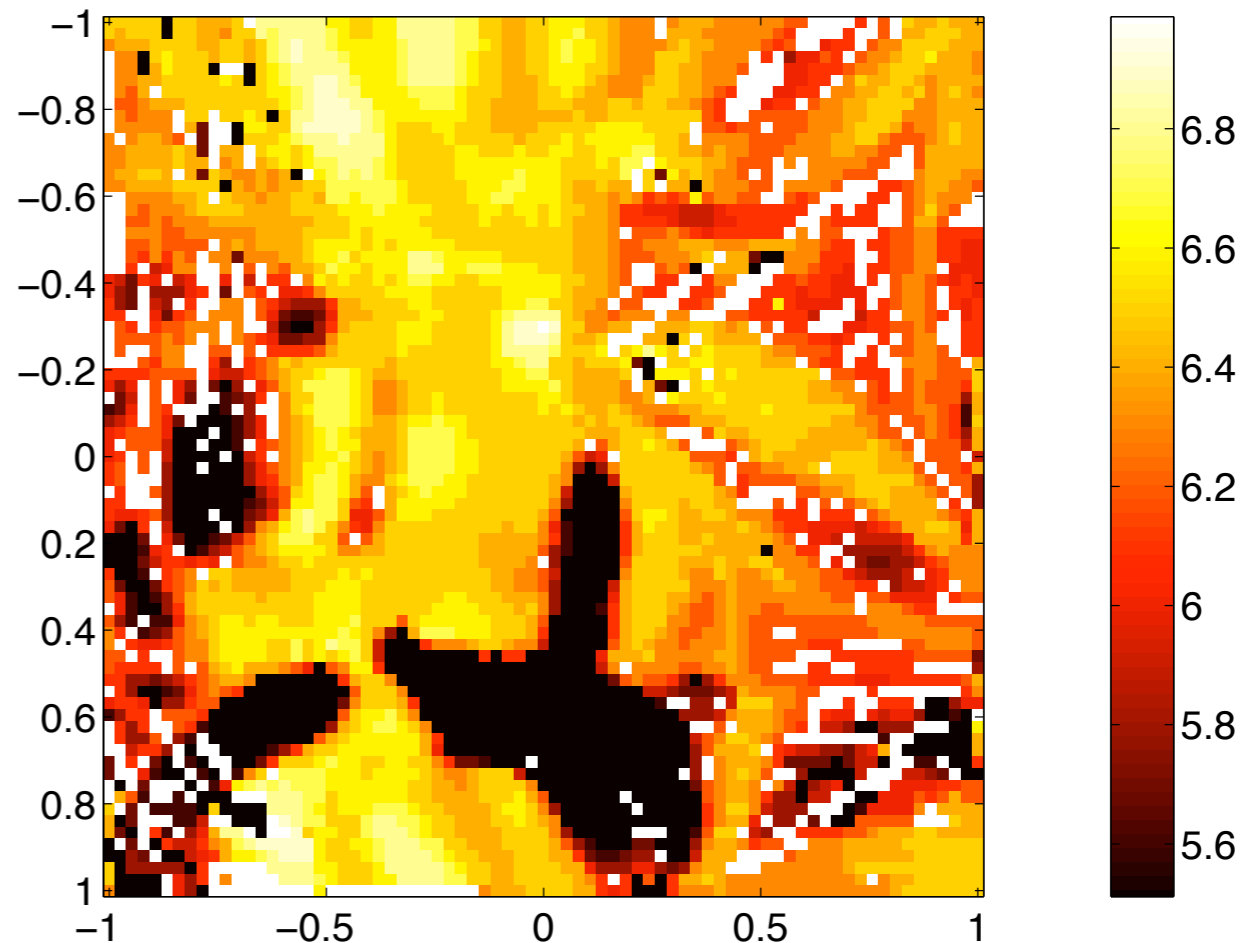
# Fe XVI (335 Å)



# Original $\text{Log}(T)$



# Reconstructed $\text{Log}(T)$



(The white streaks are due to small tomographic errors and non-uniqueness in the DEM inversion.)

# Time-Dependent Formulation of Tomographic Reconstruction

# Deficiencies of the static (time windowed) approach:

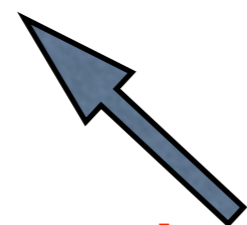
- Does not allow any type of temporal evolution, including deterministic effects, such as differential rotation (equator rotates faster than poles).
- Is poorly suited to take advantage of multi-spacecraft data sets, which have the potential to greatly increase the temporal resolution.



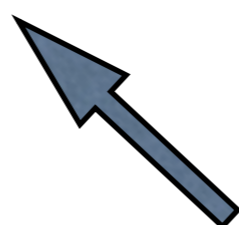
Now  $\vec{x}_t$  be a discretized version of  $N_e$  at time  $t$ .

Each vectorized image  $\vec{y}_t$  is related to  $\vec{x}_t$  via a noisy projection :

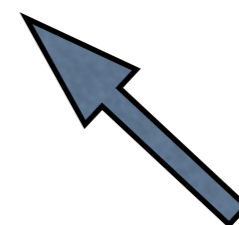
$$\vec{y}_t = \mathbf{A}_t \vec{x}_t + \vec{\gamma}_t$$



data  
vector



projection  
operator



noise  
vector

The projection eqn. is accompanied by an evolution eqn. :

$$\vec{x}_{t+1} = \mathbf{F}_t \vec{x}_t + \vec{v}_t$$



update  
operator

stochastic  
driver

When  $\mathbf{F}$  and  $\mathbf{A}$  are linear operators (as they are here), these equations are usually solved via a Kalman filter (or smoother).  $\mathbf{F}$  can be used to model simple effects such as differential rotation (i.e., the equator rotates faster than the poles) or conceivably even MHD equations.

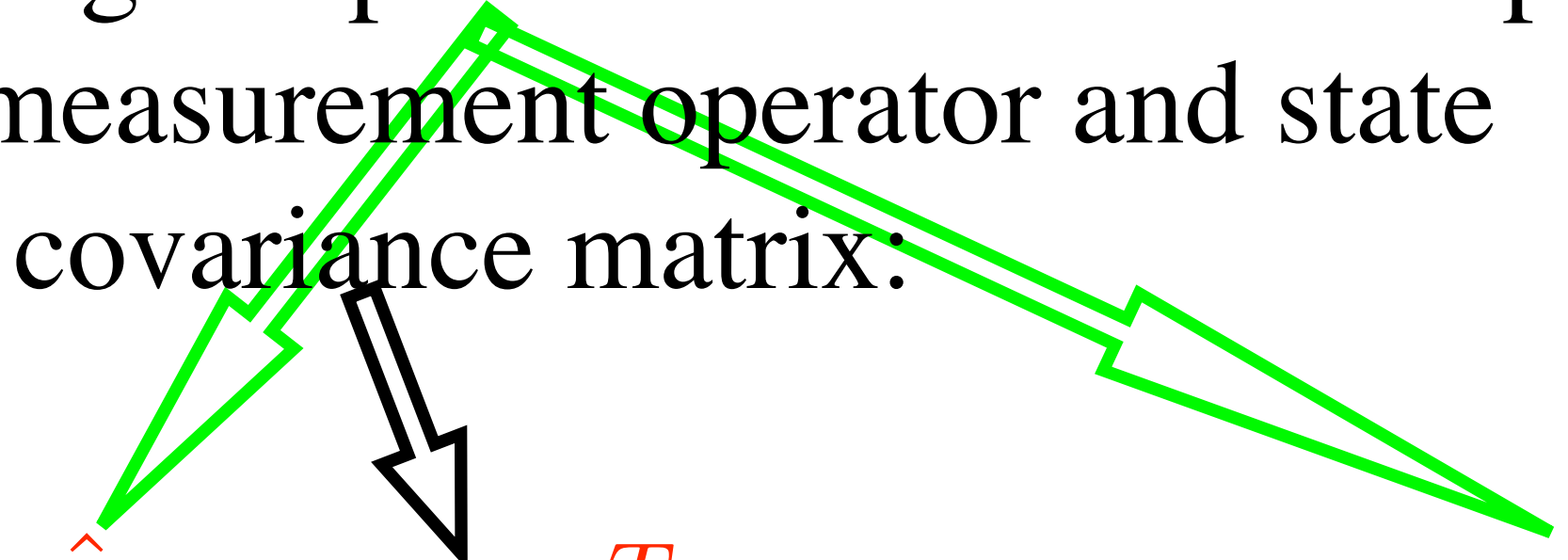
The so-called “state-space” equations are used in the weather prediction community where an estimate of the state of the atmosphere is made consistent with both observations (to within the noise) and hydro equations (to within a specified model uncertainty).

$$\vec{x}_{t+1} = \mathbf{F}_t \vec{x}_t + \vec{v}_t$$

$$\vec{y}_t = \mathbf{A}_t \vec{x}_t + \vec{\gamma}_t$$

In this case,  $\mathbf{x}$  represents the entire state of the atmosphere, and  $\mathbf{F}$  is an operator that integrates the hydro equations.

The data driven solution to the model equations is given by projecting the prediction onto the subspace defined by measurement operator and state covariance matrix:


$$\hat{\vec{x}}_{t+1} = \mathbf{F}_t \hat{\vec{x}}_t + \alpha \mathbf{C}_t a_{t+1}^T (y_{t+1} - a_{t+1} \mathbf{F}_t \hat{\vec{x}}_t)$$

where  $a_t$  is a row of  $\mathbf{A}_t$ ,  $y_t$  is one component  $\vec{y}_t$ , and  $\alpha = 1/[a_t \mathbf{C}_t a_t^T + \mathbf{E}\{\gamma_t^2\}]$

# Problem:

Kalman filter solution is computationally infeasible!

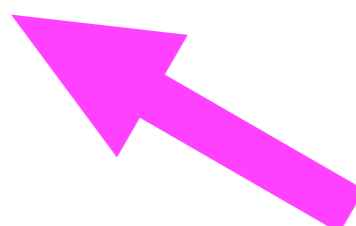
- The state vector  $X_t$  may have millions of components
- The covariance matrix of the state vector  $C_t$  will then have trillions(!) of components and cannot be stored, let alone manipulated, for KF solution.

# Our Solution:

The Localized Ensemble Kalman filter (LEnKF) [a type of unweighted Monte Carlo (particle) filter].

$P = \#$  of Monte Carlo samples of the state vector distribution.

Our estimate of the state vector is now:

$$\hat{\vec{x}}_t = \frac{1}{P} \sum_{p=1}^P \vec{x}_t^p$$


particles  
(samples)

Now, instead of being dependent on the impractical covariance matrix  $C_t$ , the estimate depends on the sample covariance:

$$\hat{C}_t^s = \frac{1}{P-1} \sum_{p=1}^P (\vec{x}_t^p - \hat{\vec{x}}_t) (\vec{x}_t^p - \hat{\vec{x}}_t)^T$$

However, this is only more computationally efficient than the standard KF when  $P \ll \dim(X_t)$ .

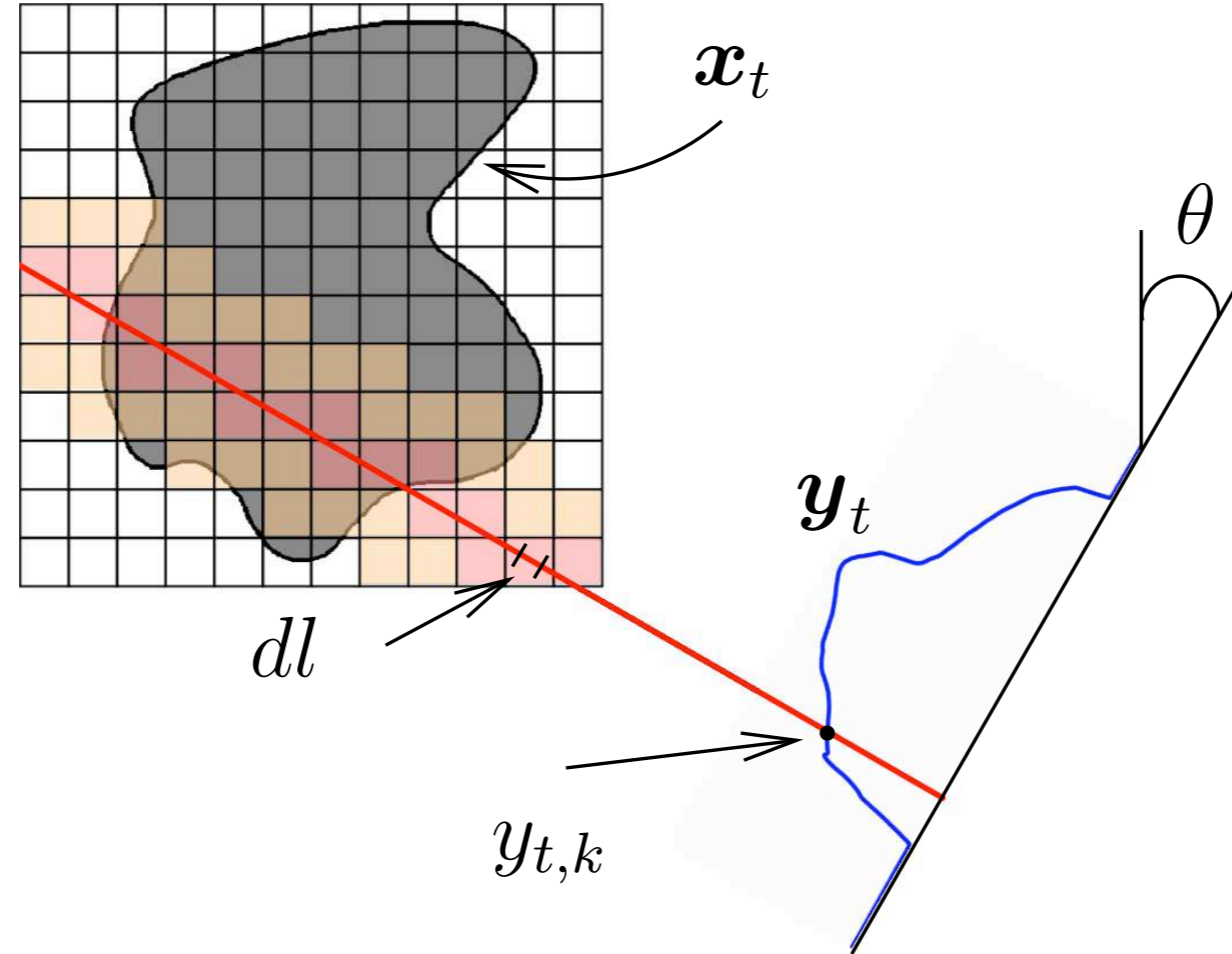
# Problem:

Under fairly general circumstances, the number of particles  $P$  required for a reasonable filter (i.e., not dominated by sample error)  $> \dim(X_t)$  and increases at least linearly with  $\dim(X_t)$ .



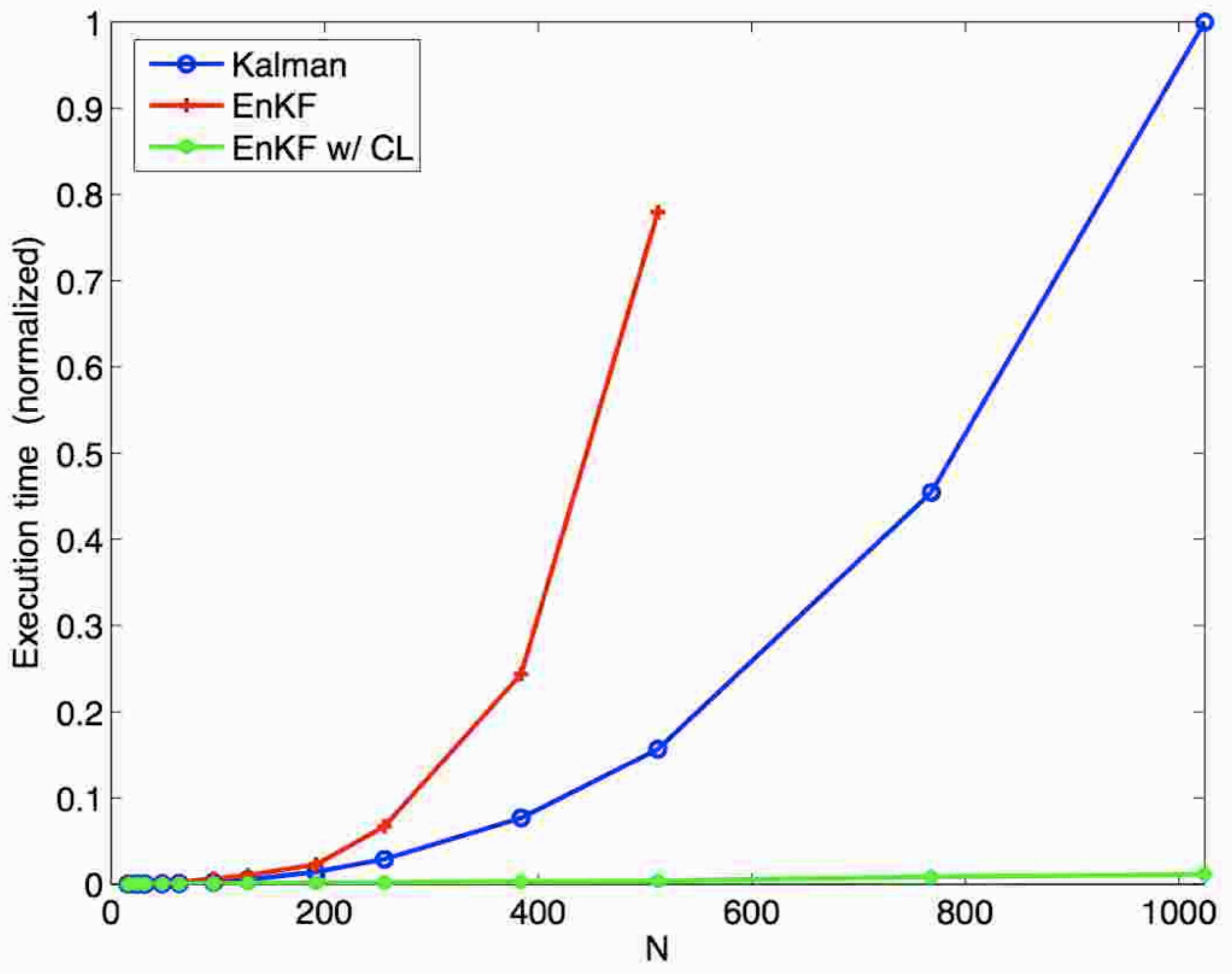
# Solution: Localization

Each (scalar) component of the observation vector  $Y_t$  contains much more information about the elements of  $X_t$  along its line-of-sight (and possibly their neighbors) than it does the far-away components of  $X_t$ .



- To a good approximation, the influence of each component of  $Y_t$  on the estimate of  $X_t$  is confined to subspace that is much smaller than  $\dim(X_t)$
- This subspace is different for each component of  $y_t$ .

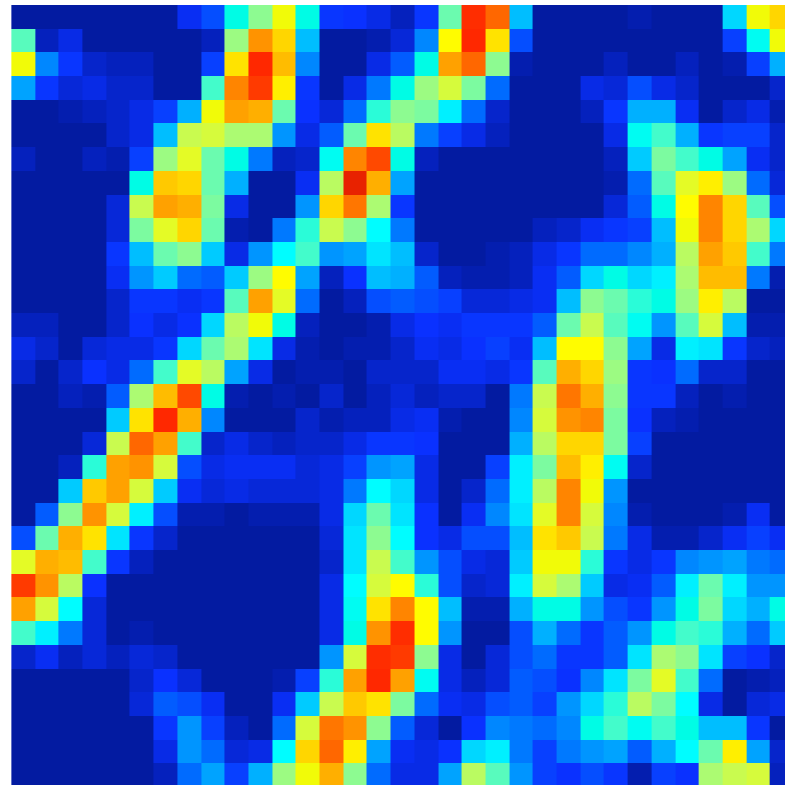
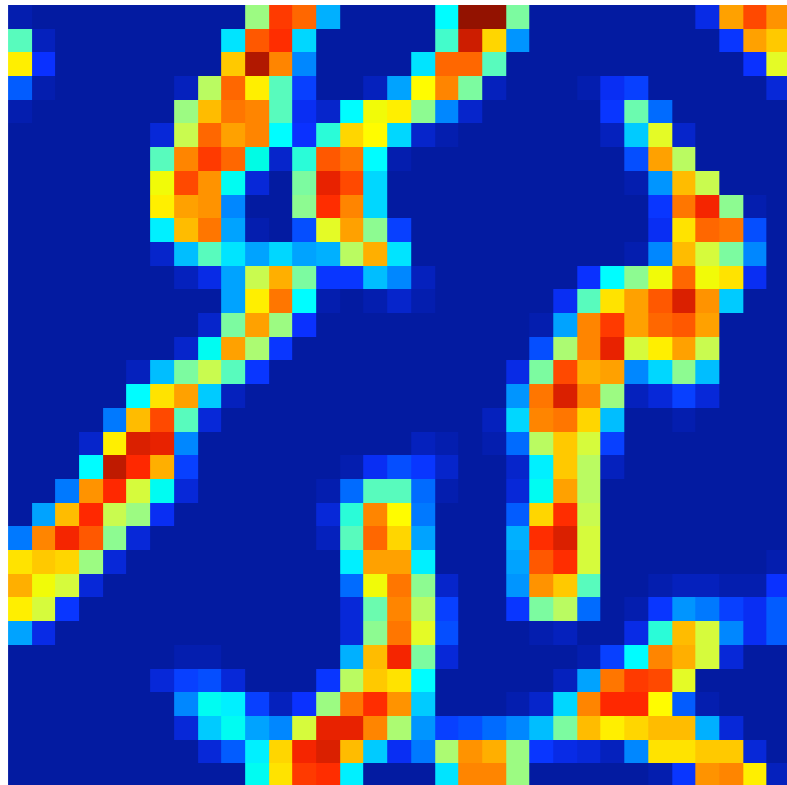
- The localized filter is applied sequentially to each of these subspaces in turn.
- E.g., if  $\dim(\vec{x}_t) = N^3$  (or  $N^2$  for 2D) then the filter need only operate on a space of dimension  $mN$ , where  $m$  is a small integer
- Thus, we have a computationally favorable framework were  $P$  is small enough



$x$ 

Kalman filter

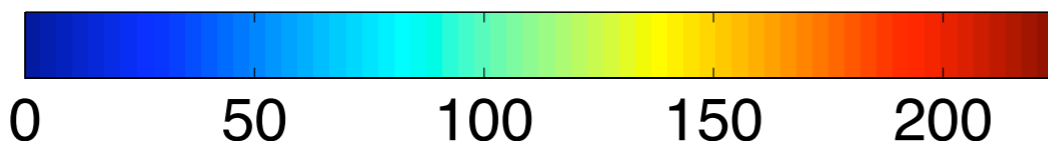
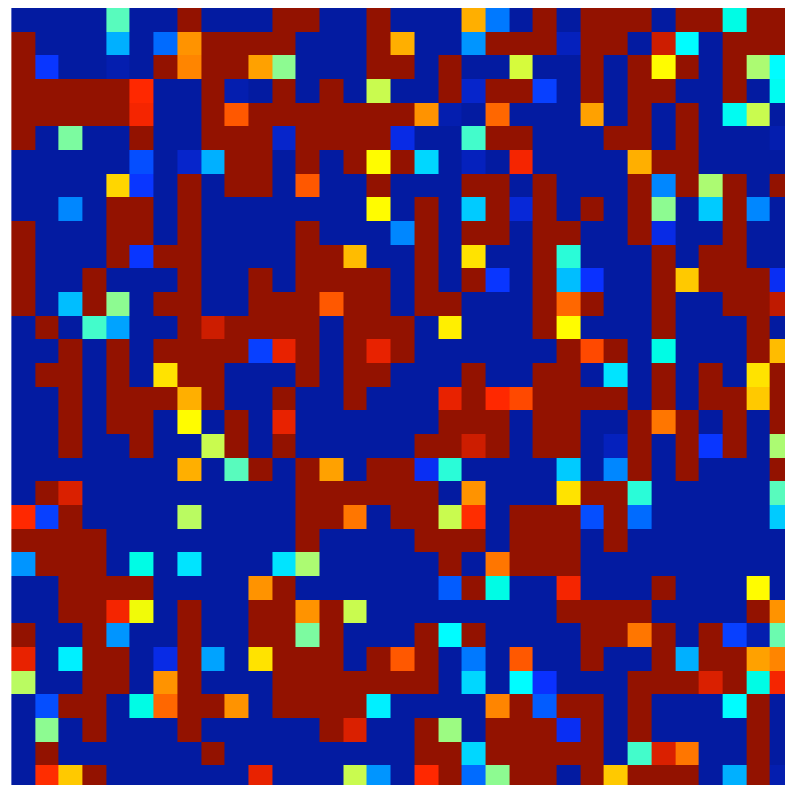
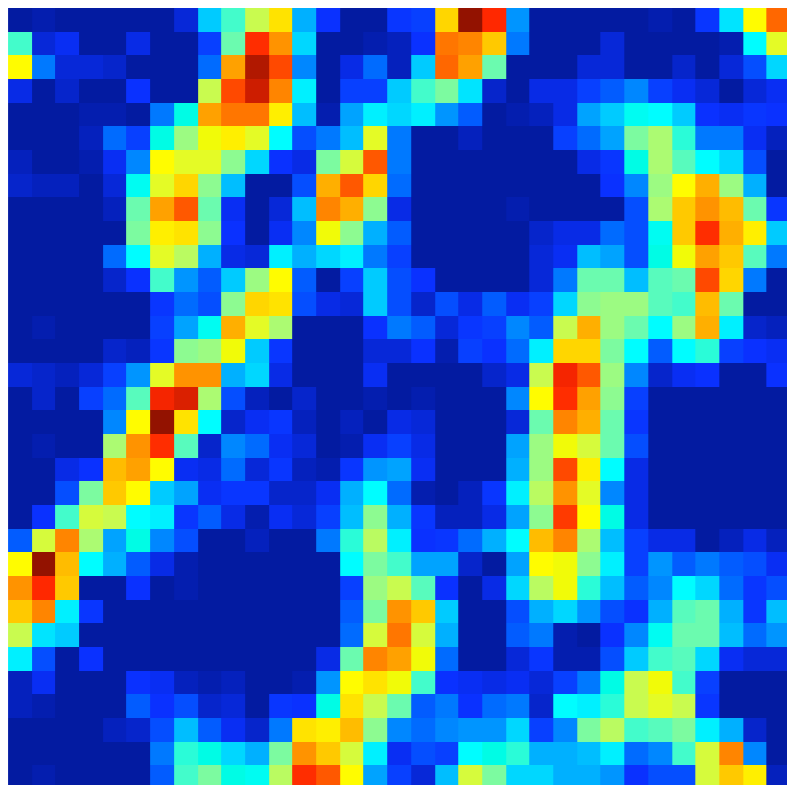
$$\dim(\vec{x}_t) = 33^2$$



Localization

No localization

$$P = 256$$



# Discussion Points

- UV diagnostics, anisotropic velocity distributions and energizing the solar wind
- Improved tomography of lab plasmas, esp. ELM's
- Weather-prediction-like combination of various observation types and hydrodynamics
- Other things

# Acknowledgments

- NASA Guest Investigator Grant
- NSF SHINE Grant
- Collaborators: Mark Butala, Yuguo Chen, Farzad Kamalabadi
- Jon Menard

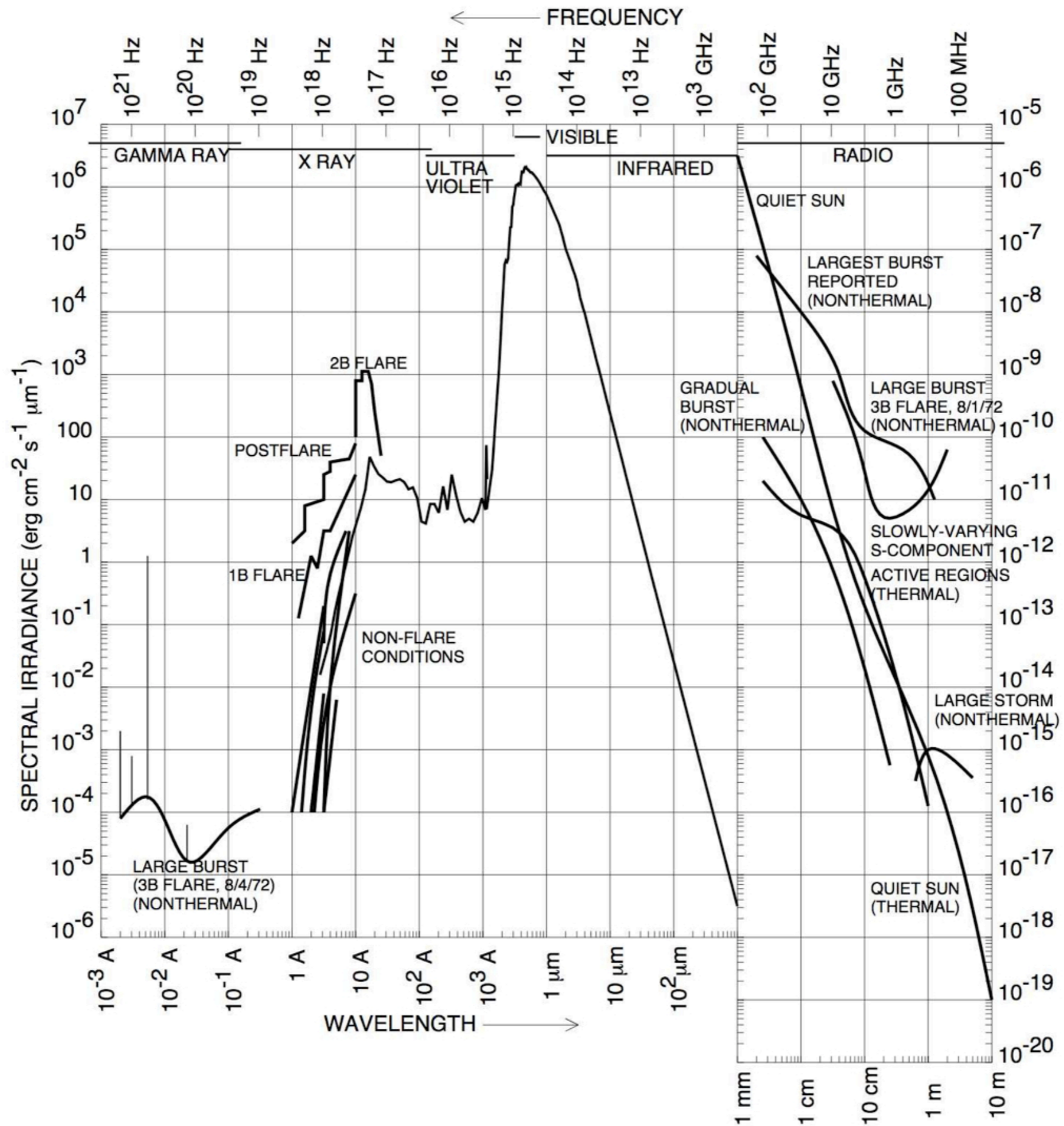


Figure 1.25: The solar irradiance spectrum from gamma-rays to radio waves. The spectrum is shifted by 12 orders of magnitude in the vertical axis at  $\lambda = 1 \text{ mm}$  to accommodate for the large dynamic range in spectral irradiance (after Zombeck, 1990 and Foukal, 1990).